Science Bulletin 63 (2018) 1141–1158

Contents lists available at ScienceDirect

Science Bulletin

journal homepage: www.elsevier.com/locate/scib

Review

Tip-induced or enhanced superconductivity: a way to detect topological superconductivity

He Wang [a,b], Lei Ma [a,*], Jian Wang [b,c,d,e,*]

[a] Tianjin International Center for Nano Particles and Nano Systems, Tianjin University, Tianjin 300072, China
[b] International Center for Quantum Materials, School of Physics, Peking University, Beijing 100871, China
[c] CAS Center for Excellence in Topological Quantum Computation, University of Chinese Academy of Sciences, Beijing 100190, China
[d] Collaborative Innovation Center of Quantum Matter, Beijing 100871, China
[e] State Key Laboratory of Low-Dimensional Quantum Physics, Department of Physics, Tsinghua University, Beijing 100084, China

ARTICLE INFO

Article history:
Received 20 June 2018
Received in revised form 23 July 2018
Accepted 24 July 2018
Available online 29 July 2018

Keywords:
Tip-induced superconductivity
Tip-enhanced superconductivity
Topological superconductivity
Point contact spectroscopy
Topological materials

ABSTRACT

Topological materials, hosting topological nontrivial electronic band, have attracted widespread attentions. As an application of topology in physics, the discovery and study of topological materials not only enrich the existing theoretical framework of physics, but also provide fertile ground for investigations on low energy excitations, such as Weyl fermions and Majorana fermions, which have not been observed yet as fundamental particles. These quasiparticles with exotic physical properties make topological materials the cutting edge of scientific research and a new favorite of high tech. As a typical example, Majorana fermions, predicted to exist in the edge state of topological superconductors, are proposed to implement topological error-tolerant quantum computers. Thus, the detection of topological superconductivity has become a frontier in condensed matter physics and materials science. Here, we review a way to detect topological superconductivity triggered by the hard point contact: tip-induced superconductivity (TISC) and tip-enhanced superconductivity (TESC). The TISC refers to the superconductivity induced by a non-superconducting tip at the point contact on non-superconducting materials. We take the elaboration of the chief experimental achievement of TISC in topological Dirac semimetal Cd_3As_2 and Weyl semimetal TaAs as key components of this article for detecting topological superconductivity. Moreover, we also briefly introduce the main results of another exotic effect, TESC, in superconducting Au_2Pb and Sr_2RuO_4 single crystals, which are respectively proposed as the candidates of helical topological superconductor and chiral topological superconductor. Related results and the potential mechanism are conducive to improving the comprehension of how to induce and enhance the topological superconductivity.

1. Introduction

Recently, topological superconductor has attracted much attention in the condensed matters physics [1–7]. Not only is it predicted to host a number of exotic physical natures [1–7], but it is also regarded as the carrier of Majorana fermions, which can be potentially applied to fault-tolerant quantum computation [8–10]. Up to now, several methods have been exploited to look for the topological superconducting state. First, by taking advantage of the superconducting proximity effect in the spin-orbital systems [11–13], the zero bias conductance peak (ZBCP) as a signature of Majorana bound state is detected [14–20]; second, by chemical doping in topological insulator system, topological superconductivity is claimed [21,22]; third, some strong spin-orbital coupling superconductors are proposed to be topological nontrivial [23–27], such as Au_2Pb [23] and Sr_2RuO_4 single crystals [24]. In this review, we will mainly introduce tip-induced superconductivity (TISC), a relatively new experimental method, which is proved to be capable of inducing and investigating the potential topological superconductivity in non-superconducting topological materials by using the hard point contact spectroscopy [28–32].

The hard point contact spectroscopy is a very useful method to study the properties of superconductors [33]. Unlike the scanning tunneling microscopy (STM) without intrusion/destruction to the sample in the probing process, the hard point contact spectroscopy would locally introduce some additional effects to the sample by the tip and may induce some exotic phenomena by modifying the properties of sample in the mesoscopic contact region

* Corresponding authors.
E-mail addresses: jianwangphysics@pku.edu.cn (J. Wang), maleixinjiang@tju.edu.cn (L. Ma).

https://doi.org/10.1016/j.scib.2018.07.019
2095-9273/

[23,28–32,34–40]. Among these phenomena, the most promising one is so-called TISC [28–32,34,35]. Here, we define the TISC as a superconductivity-like gapped feature induced by a non-superconducting tip at the point contact on non-superconducting materials. The gap is gradually removed when the temperature or the magnetic field is increased above critical value, consistent with the behavior of point contact spectra (PCS) for the superconductor. Therefore, we strongly argue that this gapped feature is TISC. As the definition implies, TISC is a phenomenon that the superconductivity is induced near or at the interface of the hard point contact between two non-superconducting materials. After the observation of unconventional TISC in three dimensional topological Dirac semimetals Cd_3As_2 [28,29], the hard point contact measurement has been employed on different topological materials to detect topological superconductivity. When it works in non-superconducting topological materials [28–32,34,35], the topological nature of these parent materials can probably be inherited by the induced superconducting states in favor of forming the topological superconducting states. For example, the TISC in Dirac semimetal Cd_3As_2 shows zero bias conductance peak (ZBCP) in PCS, which could be taken as the signature of Majorana fermions after reasonable consideration [28–30]. Compared to other methods of investigation of topological superconductivity mentioned above, the TISC method on topological materials induces the superconducting phase in non-superconducting topological materials and offers the spectroscopic information of the superconducting order parameter synchronously.

As a newly developed experimental technique based on hard point contact spectroscopy, TISC method shows its great potential in the research of topological superconductivity. Hence, in this review, besides the introduction of the basic knowledge about TISC, we will restrict ourselves to the achievement of TISC in topological materials. This review consists of five sections: Section 1 is the introduction; Section 2 starts with the basic knowledge about the point contact spectroscopy and then focuses on several typical transport characteristics of traditional point contact measurements on superconductors, which have not been fully discussed yet; the related discussion is helpful to analyze the PCS of TISC; Section 3 describes the TISC in details, including the effects from "needle-anvil" configuration and the TISC on Dirac/Weyl semimetals; Section 4 summarizes TESC for further investigation on topological superconductivity; Section 5 makes a perspective on TISC and TESC as a way to detect topological superconductivity.

2. The point contact spectroscopy

As mentioned above, either the TISC or TESC is performed by the hard point contact measurements. Therefore, the basic knowledge of point contact measurements, especially on superconductors, would be helpful for analyzing TISC or TESC. In view of this, it is necessary to give a brief introduction of the background knowledge of the point contact spectroscopy here, although the theoretical model and experimental achievements of point contact spectroscopy have already been reviewed [41–45]. After that, some typical characteristic curves of point contacts on superconductors, like the temperature dependence or the magnetic field dependence of the point contact resistance, are carefully discussed.

2.1. The classification of point contacts

The point contact is a simple constriction with radius smaller than mean free path between two materials. Since a modified structure of tunnel junction as the first point contact was realized by fabricating metallic mirco-short in the insulating barrier between two metals by Yanson [46], several types of point contacts have been developed: (i) break junction: the break junctions are fabricated by breaking samples to form the homo-contacts between two broken clean surfaces at low temperature by using a mechanical controllable system [47]. (ii) Point contact made by nanolithography: an insulating layer with a through-hole is deposited on the studied sample, where the hole with the diameter of several hundred nanometers is made by election beam lithography and dry etching; then, metal film is grown on the insulating layer and fills the hole simultaneously as a point contact [48,49]. A typical configuration is shown in Fig. 1a. (iii) Soft point contact: the soft point contact is usually created between a clean sample surface and a small drop of silver paste, as shown in Fig. 1b. The discrete silver grains in the paste touch the sample surface and form a series of parallel channels, which result in an effective contact size much smaller than the size of silver paste. The soft point contact could be mechanically and thermally stable, but the degraded surface layer of the sample near the contact interface would induce the inelastic scattering, which often broadens the conductance curves [21,44]. (iv) Hard point contact. A hard point contact is also called the "needle-anvil" configuration, as depicted in Fig. 1c, which is made between a sharp tip and a sample by pressing the tip onto the surface of sample [50]. The most kinds of the tip can be mechanically sharpened with the radius of the apex of tens of micrometers. Sharper metal tips with ending radius of the curvature of sub-micrometers can be obtained in the method of electrochemical etching.

2.2. The advantage of hard point contact

Several advantages make hard point contact become most common configuration among the methods mentioned above. (i) Tens of point contact states can be obtained in the same run of the measurement. (ii) The point contact resistance can be tuned by approaching or withdrawing the tip to the sample. (iii) The hard metal tip can pierce through the dead layer of the sample and probe the information of fresh layer. (iv) Some affiliated effects, such as doping effect, pressure effect, and interface effect, which were supposed to avoid for traditional point contact measurements but now are found to be able to induce or modulate some new physical phases near or at the contact interface.

2.3. Three regimes of point contact

In this section, we will focus on the homo-contact and model the contact as a circular orifice of radius r in a dielectric layer

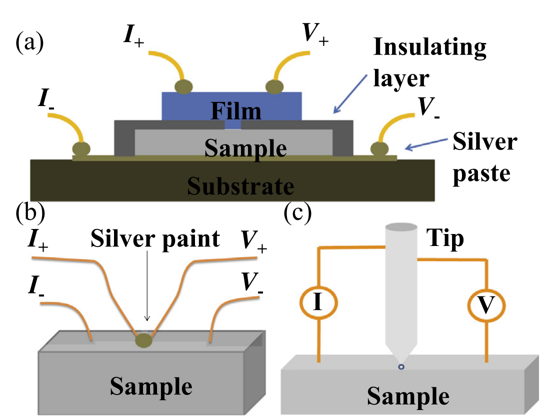

Fig. 1. (Color online) The schematics of three types of point contacts. (a) One configuration of point contact junction fabricated by nanolithography. (b) Soft point contact configuration. (c) Needle-anvil configuration, also called hard point contact configuration.

between two metals for simplicity. Depending on the comparison between the radius r of the point contact and the electron elastic (inelastic) mean free path l_e (l_i) of the sample, the point contact states can be categorized into three mesoscopic regimes: ballistic regime ($r \ll l_e$), thermal regime ($r \gg l_i$), and intermediate regime, which is between ballistic and thermal regimes.

2.3.1. Ballistic regime

When the contact radius r is much smaller than the electron elastic mean free path ($r \ll l_e$), the point contact locates in the so-called ballistic regime. In this situation, if the voltage V is applied to the contact, the electrons would be accelerated in the process of passing through the point contact without any scattering, the gained kinetic energy eV of electrons would directly reflect the energy separation between two parts of the split Fermi surface in the ballistic point contact. Thus, the point contact spectroscopy can be used as a momentum-resolved and energy-resolved spectrometer to probe the local information of Fermi surface of the sample in the contact region. The ballistic resistance was first studied by Sharvin in 1965 [51] and expressed by Sharvin resistance formula

$$R_s = \frac{4\rho l_e}{3\pi r^2}, \tag{1}$$

where ρ is the resistivity of sample. Based on the Drude model, $\rho l = \hbar k_F / ne^2$ is a constant for a particular metal, where k_F is Fermi vector, n is electron density. Eq. (1) can be further rewritten as

$$R_s = \frac{4R_q}{(k_F r)^2}. \tag{2}$$

$R_q = h/2e^2 = 12.9$ kΩ is the quantum resistance. Eq. (2) suggests that the ballistic contact resistance depends only on the contact geometry for a given materials. Moreover, the size of a clean ballistic point contact can be also calculated by using Eq. (2). When the ballistic contact consists of two simple metals, such as copper, the contact radius r can be roughly estimated as $15/\sqrt{R_s(\Omega)}$ nm [36]. In the case of point contact with finite barrier, the R_s would be rewritten as $R_{PC}/(1+Z^2)$, where Z is barrier parameter.

For a ballistic point contact between two normal metals, the Sharvin resistance gives a linear I-V characteristic, describing the ballistic injection of electrons without any scattering. But at some specific bias voltage, the electrons can be inelastically scattered back through the orifice by phonon, magnon, and so on [33,41,42]. This backflow current can further contribute a correction to the total current, leading to a measurable deviation from the linear dependence of the I-V characteristic; Surprisingly, its second derivative turns out to be proportional to the point contact electron-phonon spectral function $\alpha^2_{PC}F(eV)$, where α^2_{PC} is the averaged electron-phonon interaction matrix element with considering the influence of contact geometry, and $F(\omega)$ is the phonon density of states. Finally one obtains

$$\frac{d^2I}{dV^2} = -\frac{16er}{3\hbar v_F}\alpha^2_{PC}F(eV), \tag{3}$$

where v_F is the Fermi velocity. More generally, besides the electron-phonon interactions, the electron-electron interaction [36] and superconductivity [52] can also be characterized by the nonlinear I-V curves or the PCS.

2.3.2. Thermal regime

When the radius of a point contact is much larger than the inelastic mean free path, this point contact is in thermal regime. The homo-contact resistance in this regime is described by Maxwell resistance formula

$$R_M = \frac{\rho}{2r}. \tag{4}$$

Unlike the point contact in ballistic regime where the Fermi surface in the two electrodes has a difference of eV, the Fermi surface of a thermal point contact evolves smoothly within the contact area, and a well-defined equilibrium temperature profile is formed at the same time. In the transport process, the electrons lose most of their energy in the contact area, and contribute to the local Joule heating, which results in an increase of temperature in the contact area. The point contact temperature (T_{PC}) can be effectively expressed by

$$T^2_{PC} = T^2_{bath} + \frac{V^2}{4L}, \tag{5}$$

where T_{bath} is the bath temperature and L is the Lorenz number. For a rough estimation, when $T_{bath} \ll T_{PC}$, one can estimate the effective point contact temperature (unit of K) using the bias voltage (mV) by a factor of 3.2 K/mV [42]. And the correlation between the I-V characteristic and the temperature dependent resistivity $\rho(T)$ of the metal can be further calculated by using the formula [42],

$$I(V) = 2rV\int_0^1 \frac{dx}{\rho\left(T\sqrt{1-x^2}\right)|_{T=eV/3.63k_B}}, \tag{6}$$

where k_B is Boltzmann constant. This formula can also be used to reconstruct the $\rho(T)$ in the thermal contact area from the measured I-V curve, as shown in Section 2.6.3.

2.3.3. Intermediate regime

The intermediate regime is between the ballistic regime and the thermal regime. Its resistance can be calculated by the Wexler formula [53], which is the simple interpolation of the Sharvin resistance and the Maxwell resistance

$$R = R_S + \Gamma R_M = \frac{4\rho l_e}{3\pi r^2} + \Gamma\frac{\rho}{2r}. \tag{7}$$

Γ is the slowly varying function of the ratio l_e/r with the order of unity. Considering the extreme situation, Γ would be equal to 0 (or 1) for ballistic (thermal) regime, which means that the Sharvin resistance would be dominant if $l_e/r \gg 1$. Vice versa for the situation of $l_i/r \ll 1$, the Maxwell resistance would play a crucial role. Sometimes, people prefer to define the so-called diffusive regime during the elaboration of point contact regime. In diffusive regime, the point contact radius is larger than the elastic mean free path but still smaller than the diffusive length ($\Lambda = (l_i l_e)^{1/2}$) for the inelastic scattering. This suggests that the elastic scattering process can occur within the contact region but the inelastic scattering process is still forbidden in diffusion regime. One can expect that the PCS in this situation still contains direct energy-resolved information about the inelastic scattering of the electrons back through the orifice as that in the ballistic regime.

For a hetero-structured point contact [44], the Wexler resistance can be re-written as

$$R_{PC} = R_S + \Gamma R_M = \frac{4\rho l_e}{3\pi r^2} + \Gamma\frac{\rho_{tip} + \rho_{sample}}{4r}. \tag{8}$$

When point contact is out of the ballistic regime, both the tip and the sample contribute the finite value to the total resistance. It is noticed that Wexler formula is usually used to roughly describe the resistance of a point contact with small barrier normal to the current. That is to say, large barrier at the interface of point contact would alter the current flow and disturb the Ohm's Law current, leading to invalidation of the Maxwell term in the Wexler formula [53].

2.3.4. The magnetoresistance of a point contact out of ballistic regime

Analyzing the magnetoresistance of a point contact in intermediate regime or thermal regime is also important. Since it directly reflects the field dependence of the resistivity of sample in these regimes, it can be used for exploring the magnetic properties of sample in two aspects: (i) in the case of the point contact with small barrier ($Z \ll 1$), the magnetoresistance would be helpful for rough estimation of the size of point contact [30]. Details can be referred to Section 2.4. (ii) When the point contact is used for investigating the topological semimetal, it is easy to observe the Shubnikov de Haas oscillations (SdHOs). The analysis of SdHOs [54,55] would help determine whether the topological properties survive in the point contact.

2.4. The estimation of size of a point contact

It is hard to estimate the size of a real point contact, because of the formation of multiple channels and the existence of the barrier. However, several methods have been proposed to estimate the effective size of the point contact, and further determine what regime the point contact locates: (i) one traditional method to check whether the point contact in ballistic regime or not is to compare the l_e of sample with the radius of the point contact, which is calculated by assuming that the point contact resistance (R_{PC}) is equal to Sharvin resistance. If the point contact radius is much smaller than l_e, one can speculate the point contact is in ballistic regime, and the calculating radius is proper. Otherwise, the point contact is out of the ballistic regime and the radius of point contact must be estimated in other methods as demonstrated in the following part (ii) and (iii). (ii) If only the resistivity (ρ_s) of the sample is sensitive to temperature but the resistivity of the tip (ρ_t) is not, one can estimate the point contact radius by using the formula: $r = (\mathrm{d}\rho_s/\mathrm{d}T)/(2\mathrm{d}R_{PC}/\mathrm{d}T)$, because all the temperature dependence of the R_{PC} totally comes from the resistivity of sample [42,56]. (iii) In the case of that the field dependence of resistivity of sample is much more sensitive than that of tip, the size of point contact can also be calculated by the formula: $r = (\mathrm{d}\rho_s/\mathrm{d}H)/(2\mathrm{d}R_{PC}/\mathrm{d}H)$ [30]. And the weight of the Maxwell resistance R_M in R_{PC} can also be roughly estimated by the formula: $[\rho_s(H)-\rho_s(0)]/\rho_s(0) = [R_{PC}(H)-R_{PC}(0)]/R_M(0)$ [30]. It is noticed that the methods mentioned in this paragraph are only applicable in high transparency point contact situation, which means that the Wexler formula can be used to describe the R_{PC}.

2.5. The measurement of the PCS

Usually, the PCS mentioned in this text is the first order derivative of *I*-*V* characteristics, which is measured by the so-called "standard lock-in technique". In this technique, the supplied current consists of a small ac current i at the definite frequency ω and a DC current I ($i \ll I$). The former one is superimposed onto the latter one through an adder. If ac current i is small enough, the voltage can be expressed by the Taylor series expansion

$$V(I + i\cos(\omega t)) = V(I) + \frac{\mathrm{d}V}{\mathrm{d}I} i\cos(\omega t) + \frac{1}{4} \times \frac{\mathrm{d}^2V}{\mathrm{d}I^2} i^2 (1 + \cos(2\omega t)) + \cdots. \quad (9)$$

From Eq. (9), the first (second) order derivative $\mathrm{d}V/\mathrm{d}I$ ($\mathrm{d}^2V/\mathrm{d}I^2$) can be obtained by measuring the signal of frequency $\omega(2\omega)$ using the phase-sensitive detection. In general, the higher order terms of i are neglected due to their small values. The block diagram of this technique in our lab is shown in Fig. 2. A DC current I (supplied by Agilent B2901A) couples a small ac current i (supplied by SR7265 Lock-in amplifier) with a specific frequency through an adder box. As the

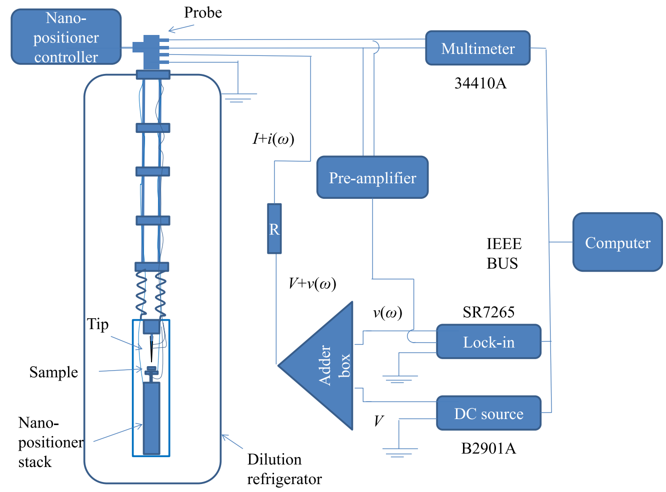

Fig. 2. (Color online) The schematic of point contact measurement by standard Lock-in technique.

measurement schematic shown in Fig. 1c, the mixed current passes through the point contact along the current path, and the DC (ac) voltage is acquired along the voltage channel by Agilent 34410A (SR 7265 Lock-in amplifier).

As shown in Fig. 3, the point contact is established in a nano-positioner system from Attocube [23,28,30,36], which is protected by a copper radiation shield. The nano-positioner stack is mounted in a home-made housing. The sample holder is fixed on the stack and the tip holder is mounted on the top of housing. One can drive the positioner to the selected position and approach the sample to contact with the tip through the corresponding controller. The coarse approaching process of AFM is used to make the point contact, instead of monitoring the vibration amplitude of tuning fork, the resistance between the tip and the sample is monitored by the external circuits; the approaching process would be ended when the measured resistance is smaller than the target value. The point contact housing is inserted into a Leiden dilution refrigerator by top-loading to obtain the cryogenic circumstance. Thus, a probe to mount the point contact housing and to load the electrical wire connecting the external circuits is designed. To reduce the heat transfer and minimize the wire resistance, the wires in the probe are designed to consist of two parts: the superconducting wires

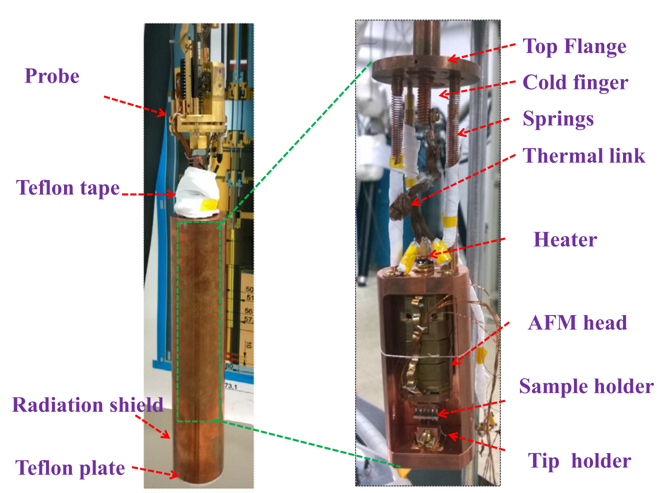

Fig. 3. (Color online) The setups of cryogenic point contact spectroscopy. The atomic force microscopy (AFM) head is mounted at the bottom of probe of dilution refrigerator by the spring system. A copper cylinder is employed as the radiation shield.

from mixing chamber to 3 K plate and phosphor bronze wires from 3 K to the end at room temperature. Both of the tip and sample are fixed to one copper housing, this would ensure that the displacement between the tip and sample is small enough to stabilize the point contact during field and temperature ramping; a suspending spring system is designed as the connection between the housing and the bottom of the probe to damp the vibration from circumstance. With those designs, a stable point contact can be obtained and measured.

2.6. Superconducting point contact

A point contact between a superconductor and a normal metal is usually called superconducting point contact. This method used to measure the superconducting gap is often referred as point contact Andreev reflection (PCAR) spectroscopy, because of the occurrence of the Andreev reflection at the interface of the point contact. In general, people take advantage of the superconducting point contact to investigate the properties of superconductors in the following aspects: (i) obtain the magnitude of superconducting order parameter from the PCS; (ii) analysis of the superconducting pairing symmetry. Using the BTK model and taking account of the order parameter of different pairing symmetry, one can theoretically get the calculated typical PCS for different pairing symmetry. This would be helpful to analyze the PCS obtained in experiments and determine the pairing symmetry. (iii) Analysis of the superconducting pairing mechanism. The second order derivative spectra give the information of quasiparticle excitations, which would be useful to analyze the pairing mechanism of the Cooper pair. (iv) Measure the spin polarization of the metal (see Section 2.6.5). Beyond these, two newly developed methods based on the superconducting point contact need to be mentioned: (a) TESC: modification of the superconducting properties. When a superconductor contacts with a normal metal tip in point contact, some additional effects like local pressure effect, doping effect, and interface effect, would also be introduced to the contact area and tune the local properties of the superconductors such as superconducting transition temperature T_c (see Section 4), in analogy to applying a pressure or chemical doping. (b) TISC: inducing novel superconducting state at the point contact between two non-superconducting materials (see Sections 3.2 & 3.3).

2.6.1. BTK theory

In the case of a ballistic superconducting point contact without barrier at the temperature much smaller than superconducting transition temperature of the superconductor ($T \ll T_c$), the contact conductance at small bias ($V < \Delta/e$) would double the value of the conductance at high bias ($V \gg \Delta/e$) as a result of Andreev reflection. In 1982, Blonder et al. [57] exploited the *I-V* curves of superconducting point contact with a barrier of arbitrary strength at the interface. The total current can be expressed by

$$I_{NS} = I_{NN}(1+Z^2)/eV\int_{-\infty}^{+\infty}[f(E-eV)-f(E)][1+A(E)-B(E)]\mathrm{d}E, \tag{10}$$

where I_{NN} is the total current of the normal metal/normal metal junction. $f(E)$ is the Fermi distribution function, the values of $A(E)$ and $B(E)$ are probability of Andreev and ordinary reflection, the quantity $[1+A(E)–B(E)]$ is referred as the transmission coefficient for electrical current. Z is a dimensionless barrier strength parameter. The PCS for different Z parameters has been calculated using Eq. (10) as shown in Fig. 4a.

The BTK theory was modified [58,59] by introducing the broadening parameter Γ which accounts for the finite quasiparticle lifetime τ ($\Gamma = \hbar/\tau$), nonzero Γ value would tend to broaden the PCS and smear the double conductance peaks to one lower conductance hump, details could refer to Fig. 4b.

2.6.2. The analysis of the PCS for superconductors.

From the measurement of the PCS at different temperatures or magnetic fields, one can obtain the temperature dependence or magnetic field dependence of superconducting gap by using BTK fitting. Fig. 5 shows that the normalized conductance curves at different T and H calculated using the BTK model of s-wave pairing symmetry. When the PCS cannot be well explained by the simple BTK theory of s-wave superconductivity, unconventional superconductivity order parameter can be considered, such as d-wave [60] or p-wave superconductivity [61]. Fig. 6 shows the calculated PCS of superconductivity with different pairing symmetry by extension of BTK model. These calculations on PCS would be helpful for analyzing the measured PCS and the superconducting mechanism.

2.6.3. The temperature dependence of ballistic superconducting point contact resistance

The sharp drop in resistance-temperature (*R-T*) curves of the point contact is usually taken as the signature of superconductivity. When the point contact is in thermal regime, the critical current effect would contribute to a resistance drop in *R-T* curves, as shown in Fig. 7b. The temperature guided by the black dashed line is corresponding to the voltage where the current through the contact area exceeds the superconducting critical current. Actually, the resistance drop can also appear in the superconducting point contact in ballistic regime with even sharper transition than that in thermal condition. In a ballistic point contact, this transition point is corresponding to the T_c of the superconductor. Sometimes, the

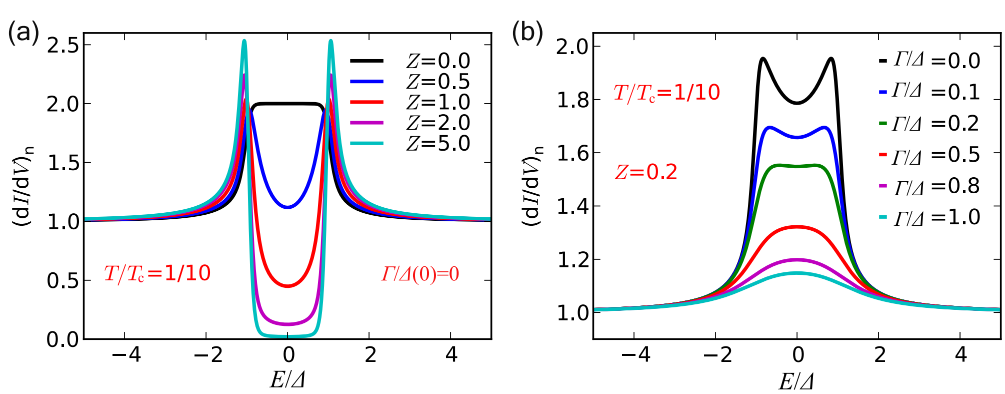

Fig. 4. Theoretical PCS for different values of the barrier parameter Z (a) and broadening parameter Γ (b) at $T/T_c = 1/10$.

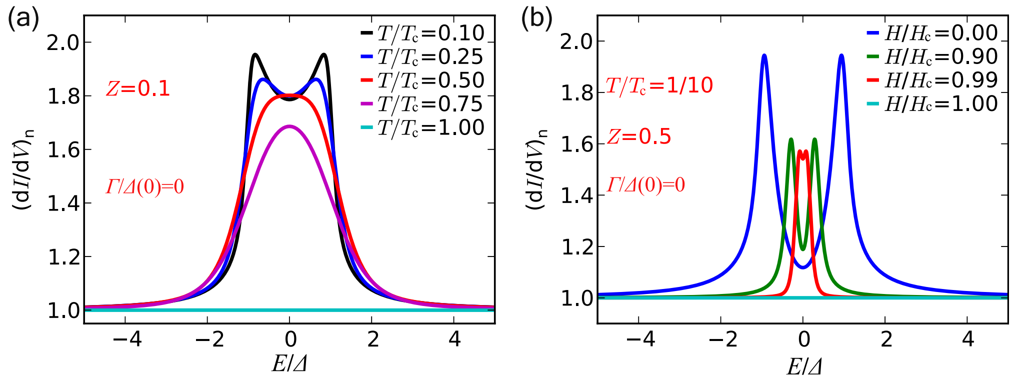

Fig. 5. Theoretical PCS for different temperatures (a) and magnetic fields (b).

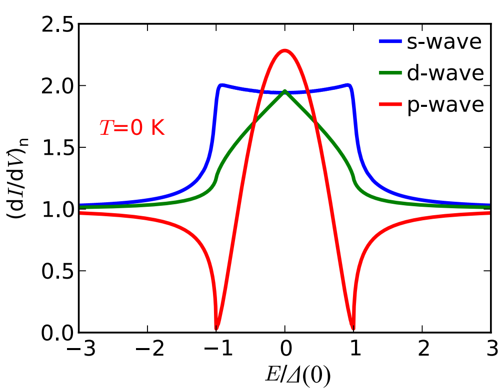

Fig. 6. The normalized PCS calculated using the extension of BTK model for different superconducting pairing symmetry: s-wave (blue, $Z = 0.1$); $d_{x^2-y^2}$ wave (green, $Z = 0.1$) and chiral p wave superconductor (red, $Z = 4$).

resistance drop in *R-T* curves cannot be observed when the superconducting point contact is in ballistic regime. There are several possible reasons for this situation, such as the thick barrier at the contact interface or the high spin polarization of spin-polarized metal.

For a ballistic superconducting point contact without barrier, the contact resistance at the temperature below T_c can decrease to half normal resistance value at $T > T_c$ as a result of Andreev reflection. Here, based on the temperature dependence of superconducting gap in BCS theory [62], the *R-T* curves with different barrier strength (Z) are calculated for a ballistic superconducting point contact with BTK model [57] (see Fig. 8a). From Fig. 8a, one can see that the resistance drop in *R-T* curves can only be observed in the situation of small barrier. Instead, when a superconducting point contact has large barrier at the interface, the *R-T* curve displays as a tunnel junction and resistance increases with temperature decreasing. Hence, if the *R-T* curve of a point contact shows no resistance transition, this does not necessarily mean that there is no superconductivity. In this case, the comprehensive analysis of the *R-T* curve and the conductance curves (dI/dV vs. V) can help to determine the existence of the superconductivity. In addition, the finite broadening parameter can suppress the resistance drop but in general cannot eliminate it as shown in Fig. 8b. The high spin polarization may also smear out the resistance drop. The detailed discussion can be found in Section 2.6.5.

2.6.4. The magnetic field dependence of a superconducting point contact resistance

Another characteristic curve of the superconducting point contact is the magnetic field dependence of the point contact resistance, also called as magnetoresistance. In the case of a superconducting point contact in ballistic regime, the magnetoresistance can tell us some important information: (i) the behavior of anisotropic magnetoresistance reflect the anisotropy of the superconducting order parameter. (ii) The transition points in magnetoresistance curves correspond to the critical magnetic field, as shown in Fig. 9. (iii) Finite barrier can induce negative magnetoresistance (see Fig. 9a).

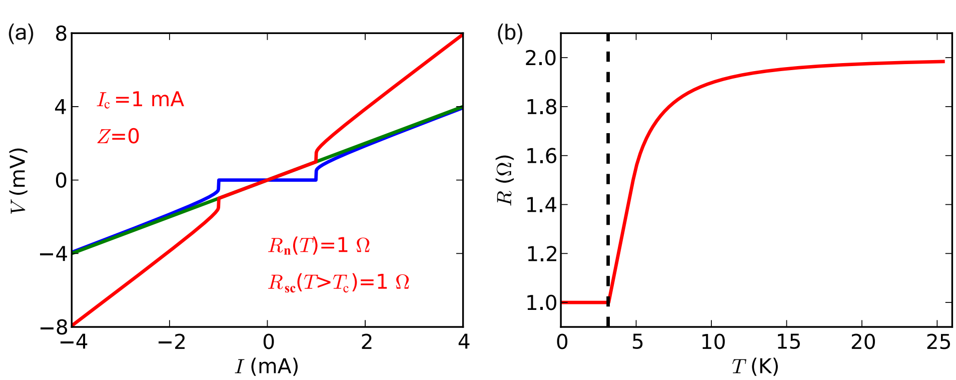

Fig. 7. The theoretically calculated curves for Maxwell resistance of superconducting point contact. (a) the *I-V* characteristic curves of normal tip (green), superconducting sample (blue) and the Maxwell resistance (red) in the case of appearance of the superconducting critical current. We set normal resistance of superconducting sample R_{sc} is 1 Ω, the resistance of normal tip R_n is 1 Ω too. (b) *R-T* curves calculated from the red curve using Eq. (6).

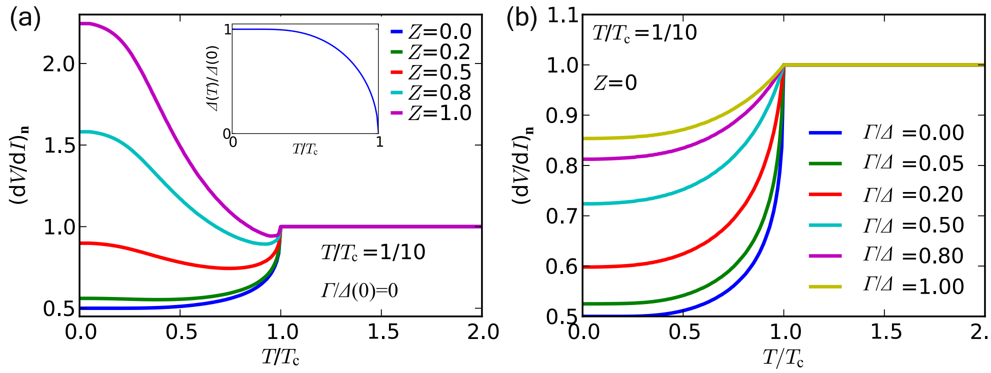

Fig. 8. The theoretical temperature dependence of PCAR resistance in ballistic regime for different barrier parameters Z (a) and broadening parameter Γ (b). Inset in (a) is standard temperature dependence of superconducting gap.

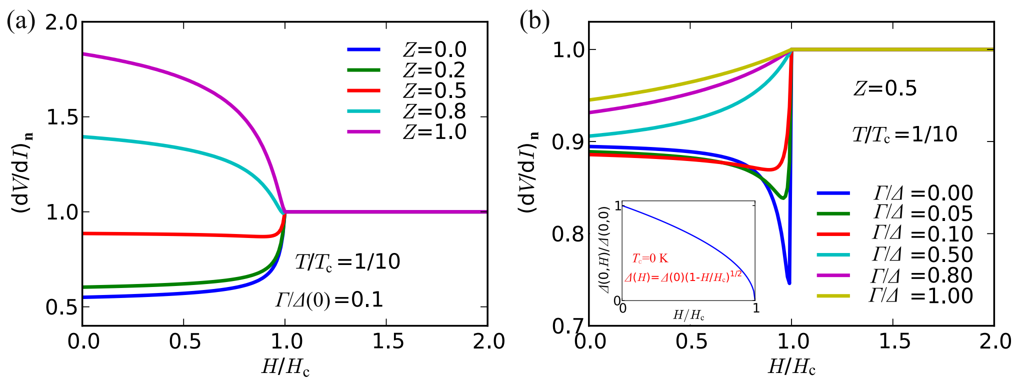

Fig. 9. The theoretical magnetic field dependence of superconducting point contact resistance in ballistic regime for different barrier parameters Z (a) and Γ (b). Inset in (b) is standard field dependence of superconducting gap at $T = 0$ K, related formula can be referred in Ref. [63].

The analysis of R-T curves also opens a new way to estimate the mesoscopic regime of a superconducting point contact. The magnetic field-free R-T curve cannot solely give enough information to distinguish the point contact in ballistic regime or not, because superconducting point contact with small barrier either in thermal regime or in ballistic regime will show a resistance drop in R-T curve. However, it would be different when the magnetic field larger than critical field of the superconductor ($H > H_c$) is applied. For the ballistic superconducting point contact, the large external field would keep the superconductor in normal state and totally suppress Andreev reflection. Because the Sharvin resistance is insensitive to the field and temperature, one can expect the point contact resistance under the large external field would keep constant in the cooling process and show little difference between the resistance with and without field at $T > T_c$. For thermal superconducting point contact under the external field above H_c, the contact resistance will show temperature dependence in the cooling process and satisfies $R(H) > R(0)$ at $T > T_c$ if the sample and tip show positive magnetoresistance at $T > T_c$.

2.6.5. Measurement the spin polarization of a metal by PCAR technique.

The superconducting point contact can be used to determine the spin polarization at the Fermi energy of a spin-polarized metal [64,65], such as ferromagnetic tip on the s-wave superconductor or superconducting tip on the ferromagnetic samples. Because the occurrence of Andreev reflection at the interface between a spin singlet superconductor and the metal under test is limited by the minority spin population near the Fermi surface. The differential conductance of the point contact can reveal the spin polarization of the metal. The current through spin-polarized point contact can be effectively considered as the sum of two parts: spin-unpolarized current and the spin-polarized current. The former one is generated in the process of Andreev reflection and obeys the BTK model; the latter one is spin polarized current carrying quasiparticles, which would suppress the total conductance for $V < \Delta/e$ (see Fig. 10a). The spin-polarized level of the current through the point contact is characterized by the parameter P, which is approximately equal to the real spin polarization of the band in the case of the absence of interfacial scattering and little difference between the Fermi velocilties of two polairzed bands. The spin polarization also exerts its influence on the R-T curve, for example, high spin polarization would smear the resistance drop in R-T curves, similar to the barrier parameter Z.

3. The tip-induced superconductivity

3.1. Introduction of the TISC

Since the first report of TISC on three dimensional topological Dirac semimetals Cd_3As_2 single crystal and poly-crystal [28,29], the TISC is taken as a newly discovered experimental method to induce superconductivity in topological materials for investigation of the topological superconductivity. The most attractive point of this method is that the superconductivity can be triggered in some specific non-superconducting sample (like Cd_3As_2 and TaAs) under a normal metal tip; this is totally different with traditional superconducting point contact measurements [33,41–45], although the theory of which can be helpful to analyze the results of TISC. Up to now, several non-superconducting materials have been explored to emerge superconducting phase under the normal metal tips

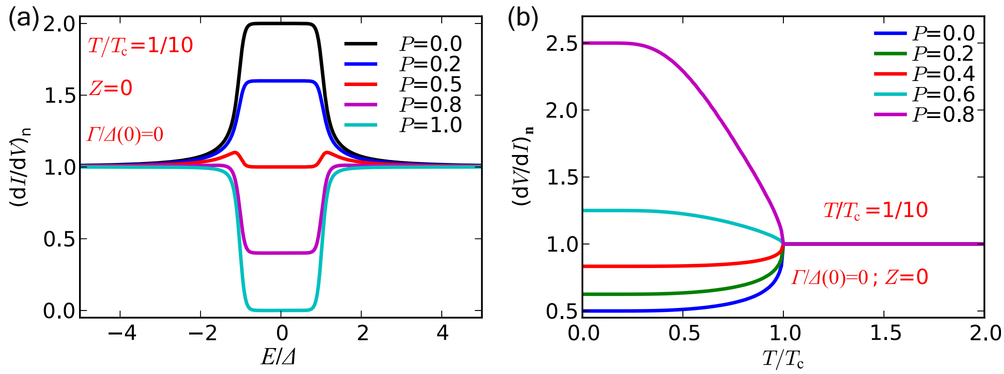

Fig. 10. The calculated PCS (a) and the temperature dependence of PCAR resistance (b) for different values of spin polarization P.

[28–32,34,35]. In the meanwhile, TISC is also investigated as a new physical phenomenon, which hosts two research focuses: the pairing symmetry and the origin of induced superconducting phase. With the progress of the TISC experiment, the former one is usually related to the nature of sample; and the later one often refers to three effects: local pressure effect, local doping effect and the interface effect. We will elaborate these three effects in next three sections.

3.1.1. Local pressure effect.

As one of the fundamental thermodynamic variables, pressure can induce superconductivity in some materials [66,67]. In hard point contact configuration, the local pressure applied by the tip to the sample may induce a new superconducting phase in the contact region due to the local enhancement of the electron-Boson coupling. The typical one is local enhanced electron-phonon coupling, which occurs in the case of increasing the local density of state or softening the local phonon mode by tuning the electron band structure of sample. This process, sometimes, is followed by the structural phase transition under pressure [38,68]. One can roughly regulate the local pressure under the tip by approaching or withdrawing the tip to the sample [36]. The maximum of local pressure can be determined by the hardness of the tip, meaning that harder tip can exert larger local pressure to the sample with less deformation. In hard point contact measurements, the common hard tips are W tip, PtIr tip, or Nb tip (Superconducting), and the common soft tips are gold tip, Ag tip, Pt tip, Fe tip (Ferromagnetic), Co tip (Ferromagnetic), Ni tip (Ferromagnetic), etc.

Unlike the hydrostatic pressure, the local pressure in the hard point contact is complicated but sometimes kind of similar to the uniaxial pressure, namely it has definite direction along the tip and normal to the surface of sample. To verify the influence of the local pressure, the soft point contact is usually chosen as a control experiment, because it is pressure-free. If the induced superconductivity by hard tip is absent when using soft point contact, the pressure effect may play a dominant role for TISC [28]. In the typical works of TISC in the Cd_3As_2 [28] and the $CaFe_2As_2$ [35], the local pressure effect exerted by the tip is usually considered as the key factor of inducing superconductivity in non-superconducting parent materials.

3.1.2. Local doping effect.

Since the first high temperature superconductor $La_{2-x}Ba_xCuO_4$ is realized by doping holes in La_2CuO_4 [69], doping has become a very common method to induce or modulate superconductivity in non-superconducting materials by intentionally introducing impurities or vacancies [70]. In the hard point contact experiment, when a normal metal tip contacts with a sample hosting very small carrier concentrations, such as semimetal, semiconductor, or even insulator, the metal tip would behave like an electron reservoir and donate the electrons to the sample. This electron transfer process can lead to the increase of local density of states of sample, which is in favor of emergence of the superconductivity. For example, the highest T_c (∼7.1 K) obtained in the TISC experiment in Cd_3As_2 single crystal [28] is obviously higher than that in pressure experiment (∼4 K) [71]. Although the local pressure effect has been proved to play a crucial role in TISC in Cd_3As_2 single crystal [28], the contribution of electron doping effect should also be deliberated in analysis of this enhanced T_c effect.

3.1.3. Interface effect

In general, the interface effect for the superconductivity refers to two aspects: one is interface enhanced superconductivity and the other one is interface induced superconductivity. The former one can be observed in FeSe film on the substrate of $SrTiO_3$ [72–76]. And the latter one is normally called "interface superconductivity" [77,78], illustrating the condition of the superconductivity triggered at or near the interface between two non-superconducting materials. The interface superconductivity can be identified as two-dimensional superconductivity when the thickness of superconducting layer is smaller than the coherence length of the superconductor. One typical interface superconductivity is observed at the interface between two band insulators, $LaAlO_3$ and $SrTiO_3$ (LAO/ STO). In the LAO/ STO system, two-dimensional electron gas is formed in a very thin layer (about 10 nm thickness) due to the confinement of the interface and becomes superconducting around 200 mK [79,80]. The interface superconductivity is also detected in $LaTiO_3/SrTiO_3$ super-lattice [81] and at the metal/insulator interface, such as $La_{1.55}Sr_{0.45}CuO_4$/La_2CuO_4 [82]. Up to now, the origin of TISC is still not fully understood. For example, although superconductivity has not been observed in TaAs under pressure [83], the TISC is discovered in Weyl semimetal TaAs single crystal [30]. Considering the interface superconductivity mentioned above, the contributions from the interface effect may play a great role in TISC in TaAs.

3.2. The TISC in 3D topological Dirac semimetal Cd_3As_2 single crystal

3.2.1. Introduction of 3D topological Dirac semimetal Cd_3As_2 single crystal

Three-dimensional (3D) Dirac semimetals, which are usually taken as a bulk analogue of graphene due to the possession of 3D linear dispersion in the electronic structure, have lately attracted increasing attention in physics and materials science [84,85]. In 3D Dirac semimetals, two Weyl points degenerate into one Dirac point, which comes in pairs under the time reversal symmetry and the inversion symmetry. Hence, in the case of either time reversal symmetry or inversion symmetry is broken, the 3D Dirac semimetal can turn into a Weyl semimetal with the Weyl points separated from the Dirac point [86,87]. In addition, 3D Dirac semimetal state has been predicated to locate in the topological phase boundary [87]; it can potentially be driven into other topological phases, such as topological superconducting states [87]. Thus, if the superconductivity is realized in 3D Dirac semimetals, one can expect that the superconducting state would host the topological properties. The realization of TISC in Cd_3As_2, a typical 3D Dirac semimetal, offers an opportunity to investigate the properties of the topological superconducting state [28,29].

Cd_3As_2, crystalizing in a tetragonal structure with space group of $I4_1cd$ with 32 formula units per unit cell [88], has been confirmed to be a kind of 3D topological Dirac semimetals by angle-resolved photoemission spectroscopy (ARPES) [89] and STM [90] experiment. The systematic research on the 3D Fermi surface of Cd_3As_2 single crystal is further explored by the measurement of angle-dependent magneto-transport [91]. The sophisticated geometry of Fermi surface of Cd_3As_2 single crystal is illustrated by the observed anomalous SdHOs behavior (Fig. 11). The ultrahigh mobility, Zeeman splitting and quantum limit properties have also been revealed by the transport measurement.

3.2.2. The discovery of TISC on topological Dirac semimetal

Up to now, abundant unusual physical properties of Cd_3As_2 single crystal have been revealed by employing variety of scientific methods [85,88–92]. One of the most striking results is the discovery of TISC in the Cd_3As_2 single crystal [28] by using the hard point contact spectroscopy. As shown in Fig. 12a, by standard four-electrode measurement the bulk shows no superconducting signal in *R-T* curves even the temperature is down to 1.8 K. Surprisingly, the superconductivity is successfully induced when a tungsten tip is pressed on the (1 1 2) surface plane of the Cd_3As_2 single crystal. Two experimental evidences shown in Fig. 12 can prove this conclusion: (i) there is a clear resistance drop at 3.9 K (see Fig. 12b), which is further suppressed to 3.7 K when a perpendicular magnetic field of 625 Oe is applied. (ii) There is a significant conductance enhancement at small bias range (±0.9 meV) in the PCS at low temperatures, which can be suppressed by applying magnetic field or increasing temperature, as depicted in Fig. 12c. The reproducibility can be supported by the fact of that these induced superconducting states are obtained with the T_c from 3.9 to 7.1 K at different point contact positions and on different samples.

3.2.3. The control experiment-soft point contact measurements

To explore the origin of the TISC is the first task after the observation of superconductivity. As mentioned above, three possible mechanisms (Local pressure, local doping and interface effect) should be considered for TISC. As a typical control experiment of TISC, a soft point contact is performed by putting a small droplet of silver paste on the (1 1 2) surface of the Cd_3As_2. Only the local dopant and the interface confinement effects should be considered carefully at the pressure-free interface of the silver grain and the sample. Several soft point contact states (see Fig. 12e, f) are detected and neither of them is superconducting. This suggests that the pressure effect may act the crucial role in the process of inducing superconductivity in Cd_3As_2 single crystal by a metal tip. This speculation is further supported by the report of uniaxial pressure induced superconductivity in Cd_3As_2 single crystal [71]. Kobayashi and Sato [93] have developed a theoretical model to study the topological superconductivity in Dirac semimetal. They claim that even the structural phase transition of Cd_3As_2 occurs under high pressure, the observed superconductivity may still be topological non-trivial due to the increase of the condensation energy protected by the combination of orbit-momentum locking effect and symmetry-lowering effect.

3.2.4. The analysis of the PCS based on a possible theoretical model

All the PCS of TISC in Cd_3As_2 single crystal contain two typical features: a zero-bias conductance peak (ZBCP) and double conductance peaks (DCPs) with double conductance dips symmetric around zero bias. Either of them exists independently of each

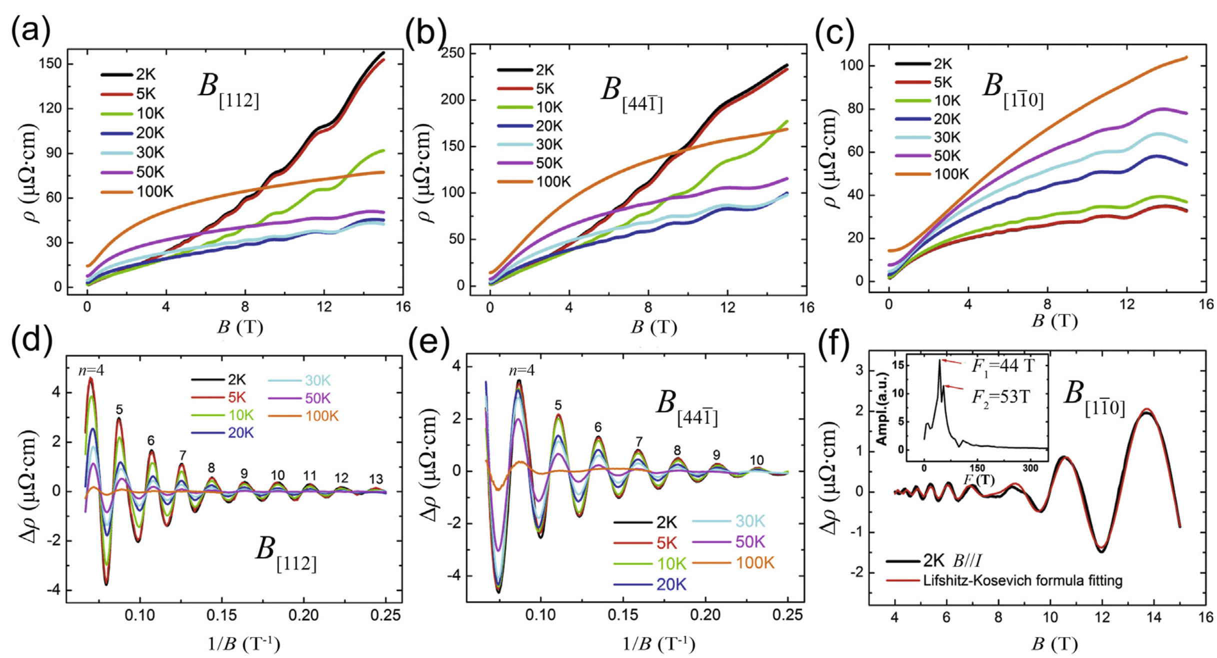

Fig. 11. SdHOs for Cd_3As_2 single crystal in different magnetic field directions, along the [112] axis (a), [44 $\bar{1}$] axis (b), and [1 $\bar{1}$ 0] axis (c) ($B_{[112]}$,$B_{[44\bar{1}]}$ and $B_{[1\bar{1}0]}$) at different temperatures. The oscillatory component of $\Delta\rho$ extracted from ρ by subtracting a fourth-polynomial background, as a function of 1/*B* at various temperatures in $B_{[112]}$ (d) and $B_{[44\bar{1}]}$ (e) directions. (f) The Lifshitz–Kosevich theory fitting to the $\Delta\rho(B)$ curve measured at *T* = 2 K in the parallel field $B_{[1\bar{1}0]}$ with two frequencies (red solid curve). Inset shows the FFT analysis with two frequencies in $B_{[1\bar{1}0]}$ direction. This figure is adapted from Ref. [91], Copyright @ 2015 American Physical Society.

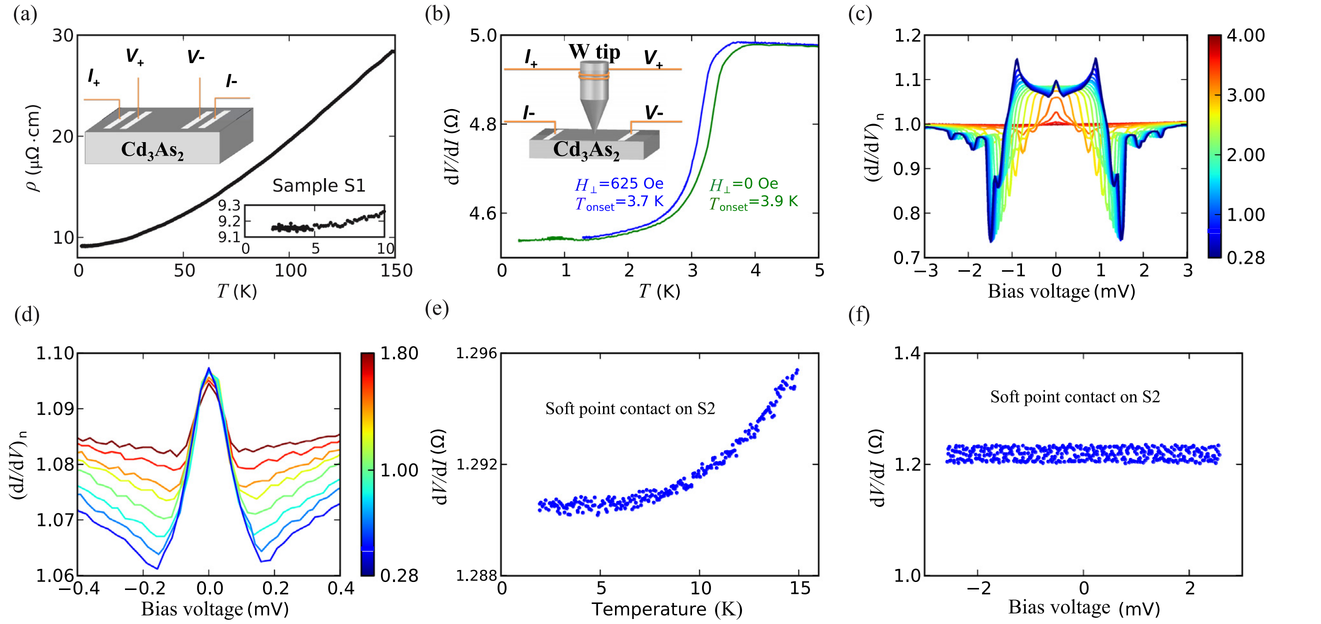

Fig. 12. Transport measurements of Cd_3As_2. (a) Temperature dependence of four-probe bulk resistivity. Upper Inset: Schematics of the standard four-probe method measurement configuration. Lower inset: Zoom-in of the resistance–temperature curve below 10 K. There is no superconductivity even $T \sim 1.8$ K (b) Temperature dependence of the zero-bias point contact resistance. Inset: schematics of the PCS measurement configuration. (c) Normalized dI/dV spectra at different temperatures varying from 0.28 to 3.8 K without an external magnetic field. The color bar corresponds to temperature. (d) Zoom-in of the normalized ZBCP. (e, f) Non-superconducting features of the Cd_3As_2 crystal measured by the silver paste "soft" point contact technique. This figure is adapted from Ref. [28], Copyright @ 2016 Nature publishing group.

other. To explain these exotic features in PCS, a theoretical model is proposed based on electron band structure of Cd_3As_2 single crystal (see Fig. 13): on the one hand, the anisotropic quasi-2D helical p-wave superconductivity (HPSC), which is formed by the intra-valley pairing mode between two bulk states of sample may account for the observed DCPs; on the other hand, the Majorana zero mode, which exists in the boundary of quasi-1D chiral orthogonal class topological superconductor (region I) induced in the helical surface Fermi arc states (FAS), may contribute to ZBCP. This is consistent with the experimental data that the ZBCP becomes sharper with decreasing temperature; although the p-wave pairing symmetry is preferred by the TISC in Cd_3As_2 single crystal, the existence of the normal s-wave superconductivity (NSC) formed by inter-valley pairing is still tolerated in this theoretical model (region II). Hence, the further identification of the topological superconductivity still necessitates more detailed experimental and theoretical studies, with the preparation of good samples and well-oriented interfaces, and will attract considerable efforts in this direction.

3.2.5. TISC in polycrystalline Cd_3As_2

The experiment of the TISC with relative soft normal metal (Ag, Au, Pt) is also performed by Aggarwal et al. [29]. Unlike the condition in Cd_3As_2 single crystal, the observed DCPs feature in polycrystalline has more broadening bias location (∼±6.5 mV) and is insensitive to the temperature and survive even up to 13 K. This is similar to the behavior of the superconducting pseudo-gap of a normal state. The difference between the results of single crystal and poly-crystal may be related to the quality of samples.

3.3. TISC found in Weyl semimetal TaAs single crystal

3.3.1. Introduction of the Weyl semimetal TaAs single crystal

Weyl semimetal is a newly discovered topological phase of matter that hosts low-energy quasiparticle excitations behaving like massless Weyl fermions, a kind of relativistic particles with definite chirality [86,94–104]. A Weyl semimetal has pairs of Weyl points with linear dispersion relations in all three momentum space directions. Two Weyl points with opposite chirality are connected only by the topological nontrivial surface Fermi arcs. Fermi arcs are non-closed surface states and serves as a path for Weyl fermions pumped between two Weyl points of opposite chirality when the magnetic and electric fields are parallel applied. This phenomenon is the so-called chiral anomaly, which exhibits negative longitudinal magnetoresistance in the transport measurements due to the Berry curvature effect [86,94–104].

As the firstly experimental confirmed Weyl semimetal, TaAs crystal possesses the inversion symmetry breaking Weyl semimetal state with 12 pairs of Weyl points in the momentum space, which are topologically protected against small perturbations [86,94–104]. The TISC in TaAs for the first time was reported by Wang et al. in *arXiv* on July 2, 2016 [30] using a PtIr tip. Compared with the Dirac semimetal, Weyl semimetal hosts pairs of Weyl points with definite chirality and intrinsically topological Fermi surfaces [86,94–104]. This essential difference may make the Weyl semimetal be a better platform to induce topological superconducting states and realize Majorana fermions, which have potential applications to fault-tolerant topological quantum computation.

3.3.2. The TISC in Weyl semimetal TaAs

On the one hand, the nature of sample [30] is characterized in four aspects: (i) the quality of the samples. The high-quality nature of TaAs single crystals, which are grown by chemical vapor transport method, is characterized by atomically high-resolution transmission electron microscopy. (ii) The sample is non-superconducting itself. The metallic-like behavior is demonstrated by the temperature dependence of bulk resistivity down to 2 K measured by standard four electrodes configuration. (iii) The observation of negative magnetoresistance induced by chiral anomaly. This confirms that the sample hosts the crucial transport signature for Weyl fermions in Weyl semimetal states. (iv) Topological nontrivial property. The π Berry's phase of TaAs crystal

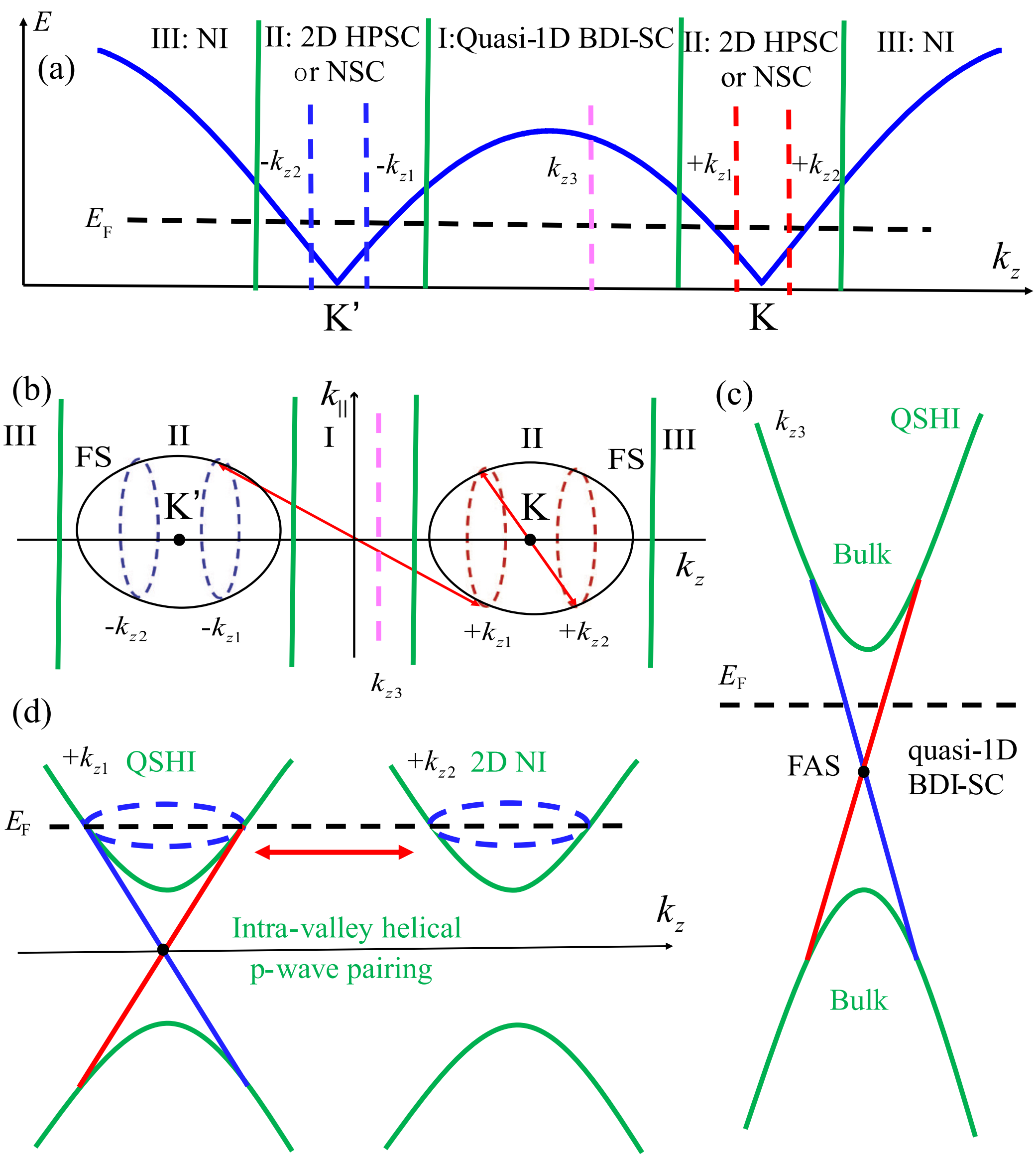

Fig. 13. Topological phase diagram for superconducting Cd_3As_2. (a) The phase diagram consists of three regions: quasi-1D BDI-SC in the surface, quasi-2D HPSC or NSC (bulk), and normal insulator (NI) (bulk). The transitions between them are marked with green lines. Blue, pink and red dashed lines indicate some particular momentum values in the different regions. (b) Fermi surface with different k_z slices. The ovals imply the anisotropic Dirac cones at the two Dirac points, with the Fermi velocities being different along k_z and the transverse directions. Each red arrow denotes two states in the Fermi surface which form Cooper pairs. The green solid, blue, pink and red dashed lines are the same as in (a). (c) Schematic diagram of the pairing between FAS (denoted by blue and red lines) in region I, which gives rise to quasi-1D BDI-SC with Majorana zero modes. The green curves represent the bulk spectra, and the black dashed line is the Fermi energy. (d) Schematic diagram of intra-valley pairings in region II, which results in the quasi-2D HPSC. The blue dashed curves are the same as in (b). This figure is adapted from Ref. [28], Copyright @ 2016 Nature publishing group.

associated with Weyl fermions is further supported by analysis of SdHOs. From the above information, the TaAs crystal used for TISC can be identified as high-quality Weyl semimetal. On the other hand, the TISC is detected in the hard point contact experiment, in which the PtIr tip is pressed on the (0 0 1) surface of the TaAs single crystal. Significant resistance drop in temperature dependence of the point contact resistance and the clear conductance enhancement in PCS are observed in some point contact states, which can be suppressed by applying magnetic field or increasing temperature, according with the typical behaviors of superconductivity.

3.3.3. To determine the mesoscopic regime of the point contact

The mesoscopic regime of the point contact can be determined according to the experimental data. As the discussion in Section 2.4, when the sample is in normal state, the temperature or magnetic dependence of the point contact resistance can help estimate the contribution of the Maxwell resistance to total point contact resistance. Since the Sharvin resistance is independent on the temperature or magnetic field, the variation of point contact resistance in normal state totally comes from the Maxwell resistance. In the low temperature and small magnetic field condition ($T < 10$ K, $H < 3$ T for TISC states shown in Fig. 14), the obvious variation can be only observed in the magnetic dependence of the resistivity of TaAs; and its temperature dependence tends to saturate in temperature dependence. Thus, the point contact magnetoresistance curve in normal state can help analyze the contribution of the Maxwell resistance to the total point contact resistance, and the analysis method mentioned in Section 2.4 is adapted. Based on the assumption that the magnetoresistance of TaAs in the contact area changes little under the applied pressure from the tip, the calculated ratio between the Maxwell resistance and the Sharvin

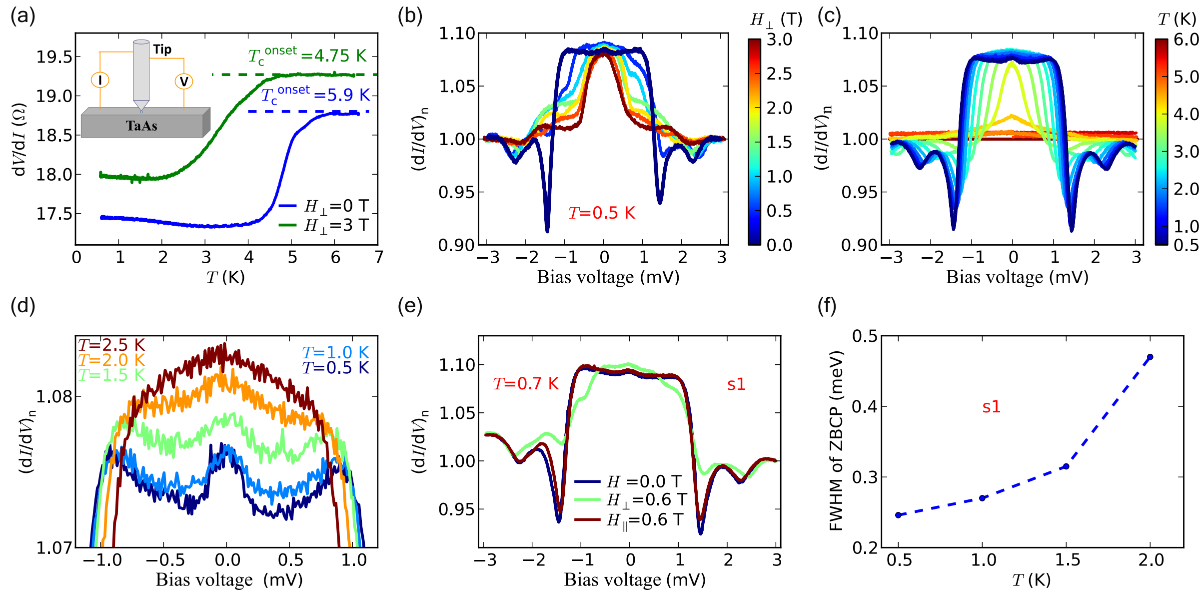

Fig. 14. Point contact measurements between a PtIr tip and the TaAs crystal. (a) Temperature dependence of zero-bias point contact resistance. (b) PCS at 0.5 K under different magnetic fields normal to the sample surface. (c) PCS at selected temperatures from 0.5 to 6.0 K. (d) Zoom in of the normalized ZBCP. (e) PCS under in-plane and out-of-plane magnetic fields showing anisotropic property of the tip induced superconductivity on a TaAs crystal at $T = 0.7$ K. (f) FWHM (full width at half maximum) of ZBCP in (a). This figure is adapted from Ref. [30], Copyright @ 2017 Science China Press.

resistance is about 0.066%, suggesting this point contact is very close to the ballistic limit. Detailed calculation can be referred to the supplementary file of Ref. [30].

3.3.4. The PCS under the external magnetic field

The PCS shows very obvious anisotropic field dependence. On the one hand, as shown in the Fig. 14b, the conductance plateau with double peaks is gradually suppressed to multiple step-like features with increasing the magnetic field normal to the sample surface at 0.5 K, consistent with the results of *R-T* curves shown in Fig. 14a. On the other hand, when field is applied parallel to the (0 0 1) surface of sample, there is much less influence on the PCS compared to that under the perpendicular field with same value, indicating critical field in parallel is much larger than the perpendicular one. The anisotropy of the TISC states gives two conclusions: (i) extraordinary large parallel critical field at zero temperature. From the temperature dependence of the point contact resistance shown in Fig. 14a, the perpendicular critical field at zero temperature can be estimated as about 8.53 T by the formula $H_{c2}(T) = H_{c2}(0)[1-(T/T_c)^2]$ with $T_c = 5.9$ K and $H_{c2}(4.75\text{ K}) = 3$ T; Hence, one can expect the parallel critical magnetic field at zero temperature is much larger than 8.53 T, and should exceed the Pauli limit for weak-coupling BCS superconductor ($H_p = 11$ T), estimated by the formula $H_p = 1.86\,T_c$. (ii) The highly anisotropic magnetic field dependence (as shown in Fig. 14e) reflects the anisotropy of superconductivity, indicating the possibility of unconventional superconductivity. This would be helpful to analyze the origin of the TISC. Combining these two conclusions, the spin-orbit coupling or scattering do affect the superconductivity and produce the component of p-wave pairing, which is reminiscent of Zeeman protected superconductivity in 2D system with the in-plane magnetic critical field much larger than Pauli limits [105,106].

3.3.5. Analysis of the PCS

All the observed PCS show two typical features: the zero bias conductance peak (ZBCP) as well as a conductance plateau with double conductance peaks and sharp double dips symmetric to the zero bias voltage (see Fig. 14c and d). Either of them may originate from several mechanisms, however, the most likely mechanism can also be distinguished based on the combination of experimental data and the nature of the TaAs. Detailed analysis would be discussed in the following paragraphs.

ZBCP in PCS can be attributed to several mechanisms, which are introduced in details by Sasaki et al. [21]. Here we will focus on the analysis of the potential mechanism of the ZBCP obtained in point contact on TaAs: first, the Kondo effect can be excluded by the absence of split of ZBCP under the external magnetic field; second, the ZBCP would broaden or split into double peaks with temperature decreasing, if it arises from a new superconducting state. Whereas both of them are absent in PCS at different temperatures, the possibility of this scenario can also be eliminated. From the Fig. 14f, it is easy to see that the ZBCP becomes sharper with decreasing temperature, consistent with the signature of Majorana Fermions in the boundary state of the topological superconductor.

In the PCS, the feature of the double conductance peaks with double conductance dips can be observed in several conditions. One of the most common conditions is a point contact in the intermediate regime, where double conductance peaks are caused by Andreev reflection with finite barrier and double conductance dips are induced by the decrease of critical current due to the local heating in the point contact region [107]. As discussed in Section 3.3.3, since the ratio R_m/R_{sh} is only about 0.066%, which is much smaller than 1, the contribution from Maxwell resistance for the total point contact resistance ($\approx R_m + R_{sh}$) is so little that the critical current cannot work in this condition.

Another possible condition is that an unconventional superconductor with d-wave or p-wave pairing symmetry appears under the point contact. Similar to the experimental results in Cd_3As_2 single crystal [28], the PCS of TaAs single crystal also shows simultaneous appearance of the ZBCP, double conductance peaks, and double conductance dips. Although any of these three features in PCS has its possible trivial origin, all three features have not been simultaneously observed in conventional superconductors so far. The scenario which can contains these three typical features in the same PCS is most likely p-wave superconductivity. Considering the nature of the TaAs, a minimal model of a novel mirror-symmetry protected topological superconductor induced in TaAs is proposed. In this model, the topological non-trivial superconductivity supports p-wave pairing.

3.3.6. The minimal model on TaAs

During the process of establishing a theoretical model to seek for the potential nontrivial topological superconducting state, two properties of TaAs must be taken into consideration: (1) 12 pairs Weyl points of TaAs (see Fig. 15b) are related by mirror and C4 symmetries. When TISC is realized on the (0 0 1) surface, the mirror symmetries along x (M_x) and y (M_y) axis can be preserved. Considering the particle-hole redundancy, M_y is selected to be $is_y\tau_z$, which is different with $M_x = is_x$. (2) TaAs is a time-reversal invariant Weyl semimetal, thus the superconducting pairing must occur between two Weyl cones as time reversal partners for each other. Hence, TaAs can become a 3D fully gapped mirror topological superconductor with odd parity superconducting order by respecting both time-reversal and mirror symmetries. The boundary of superconductor contains Majorana surface Dirac cones, whose numbers can be described by the mirror invariant. The finite bias double conductance peaks and double conductance dips can be seen in the calculated tunneling spectra due to the Majorana surface states (as shown Fig. 15a), and the ZBCP can be further obtained when coupling strength between the surface modes and the tip is weak, such as $\delta = 0.01$.

3.3.7. The origin of the TISC in TaAs

To analyze the origin of TISC in TaAs, the chance of pressure-induced superconductivity is small on account of no evidence of superconductivity observed in the pressure experiment on TaAs [83]. However, this does not mean the contribution from the local pressure to the TISC can be totally neglected. The highly anisotropic magnetic dependence of the TISC state is a clue pointing to the interface superconductivity, which is often observed in 2D or quasi 2D superconducting system, such as LAO/ STO [108]. Nevertheless, more experimental evidences are necessary to support this scenario in TISC experiment in TaAs. With these uncertainties, it is difficult to give a definite origin of TISC in TaAs based on the current experimental data. Hence, it is still calling for more experimental efforts to seek for the answers to this question.

3.3.8. TISC on TaAs using soft tips

Soon after the discovery of TISC on TaAs by Wang et al. [30], superconductivity was also reported by Aggarwal et al. [31] using soft sliver tip. Instead of the topological superconductivity, the surface spin polarization is introduced to interpret the suppression of the conduction enhancement at the bias smaller than superconducting gap. The difference between the interpretations of these two works has not been clearly understood until now. However, the debate on the mechanism of TISC calls for more elaborate experiments and theories to further investigate on this issue.

4. Tip enhanced superconductivity in candidate of topological superconductors

4.1. Introduction of tip enhanced superconductivity

In a point contact, the properties of sample can be locally modified in the contact area by the metal tip. This local modification may exhibit various novel phenomena: (i) the tip-induced new phase. In this condition, some new properties, which are absent in both tip and sample, are obtained around the point contact region, such as TISC [28–32,34,35], spin-valve effect [40], or structural phase transition [38]. (ii) Tip enhanced/suppressed superconducting properties. For example, the superconducting critical magnetic field (H_c or H_{c2}) of some superconductors in point contact measurement shows larger or smaller value than that of bulk superconductor due to the local modification exerted by the tip. In some cases, the H_c or H_{c2} of superconductor (such as Zn) under the tip is suppressed due to the demagnetization effect arising from the geometry of the point contact [39]. In some other cases, the H_c or H_{c2} in the dirty-limit superconductors is enhanced because of a short mean free path resulted from the local disorder or defects in the contact area introduced by the tip [39].

As well as the superconducting critical field, the superconducting transition temperature (T_c) under the tip can also be locally modified, which can be observed in point contact experiment on pressure sensitive superconductors. The pressure from the tip can change the band structure of the sample, ultimately leading to modification of the electron-phonon coupling strength. When the electron-phonon coupling is weakened due to the decrease of the density of state or the shift of the phonon spectrum to higher frequencies [67], the T_c would shift to lower value with the higher pressure applied, this can be called as pressure-suppressed superconductivity, which is common in conventional superconductors [109]. Besides, sometimes the suppressed T_c is observed in point contact measurements due to the surface degradation of the studied superconductor [45]. On the other hand, the pressure-enhanced superconductivity can be realized by hard point contact measurement in the case of enhancement of the electron-phonon coupling by pressure. In fact, any effect that can increase the

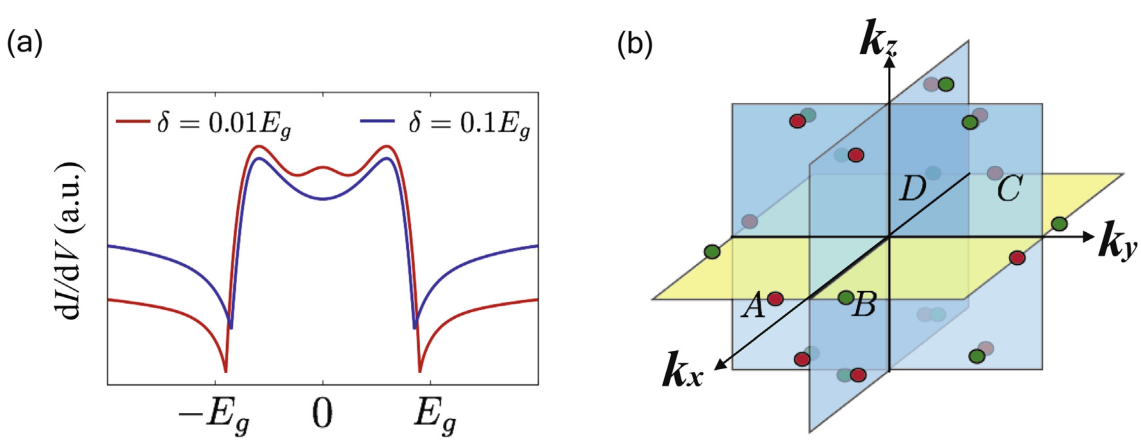

Fig. 15. Theoretical interpretation of the experimental observation. (a) The tunneling spectra at temperature much lower than T_c. (b) The sketch of the Weyl points in TaAs. This figure is adapted from Ref. [30], Copyright @ 2017 Science China Press.

density of states and electron-phonon coupling would enhance T_c, such as doping effect and interface effect, which also exist in hard point contact configuration.

In this section, we focus on the phenomena of the T_c enhancement under the tip, called as tip-enhanced-superconductivity (TESC), in the candidates of helical topological superconcdcutor-Au_2Pb [23] and chiral topological superconductor-Sr_2RuO_4 [24]. The main results are introduced in the following text.

4.2. The TESC in Au_2Pb single crystal with tungsten tip.

The investigation of the superconductivity of Au_2Pb has been reported as a kind of new superconducting compound in 1965 [110]. Recently, it attracts tremendous interest because of the predication of topologically nontrivial Z_2 invariant [111] and the interesting transport results [23,111–113]. The cubic Laves phase Au_2Pb exhibits the signature for the symmetry-protected Dirac semimetal state at temperature $T > 100$ K; Then it undergoes the structure phase transition upon cooling down to lower temperature $T < 100$ K, meanwhile, opens a gap at Dirac cone, and finally becomes superconducting below 1.2 K. Combination of the superconductivity and the potential existence of topological surface states makes Au_2Pb a good candidate of helical topological superconductors. The finite triplet contribution to the pairing state in Au_2Pb is further confirmed by the electrical transport measurement, where the temperature dependence of the reduced critical field is close to that of polar p-wave state [23].

In the point contact measurement, different tips are used to create point contacts on the (1 1 1) surface of the Au_2Pb single crystal. One relative soft tip is mechanical sharpened from 0.5 mm diameter gold wire. The T_c (1.13 K, shown in Fig. 16a and c) and H_{c2} (H_{c2}(0.5 K) ~0.02 T, shown in Fig. 16e) revealed by the point contact measurement with a gold tip are consistent with that obtained in the bulk transport and magnetization measurements (T_c - ~ 1.15 K, H_{c2} (0.18 K) ~0.05 T, see Fig. 17a and b), which demonstrates our hard point contact measurement setup is reliable for studying superconductors. The other relative hard tip is prepared by electrochemical etching method with a tungsten wire of 0.25 mm diameter. Surprisingly, both the T_c and H_{c2} are remarkably enhanced to the value of 2.1 K and 0. 6 T measured at 0.5 K, respectively (see Fig. 16b, d and f). The latter one is 10 times larger than the bulk value. The superconducting gap is also enhanced and

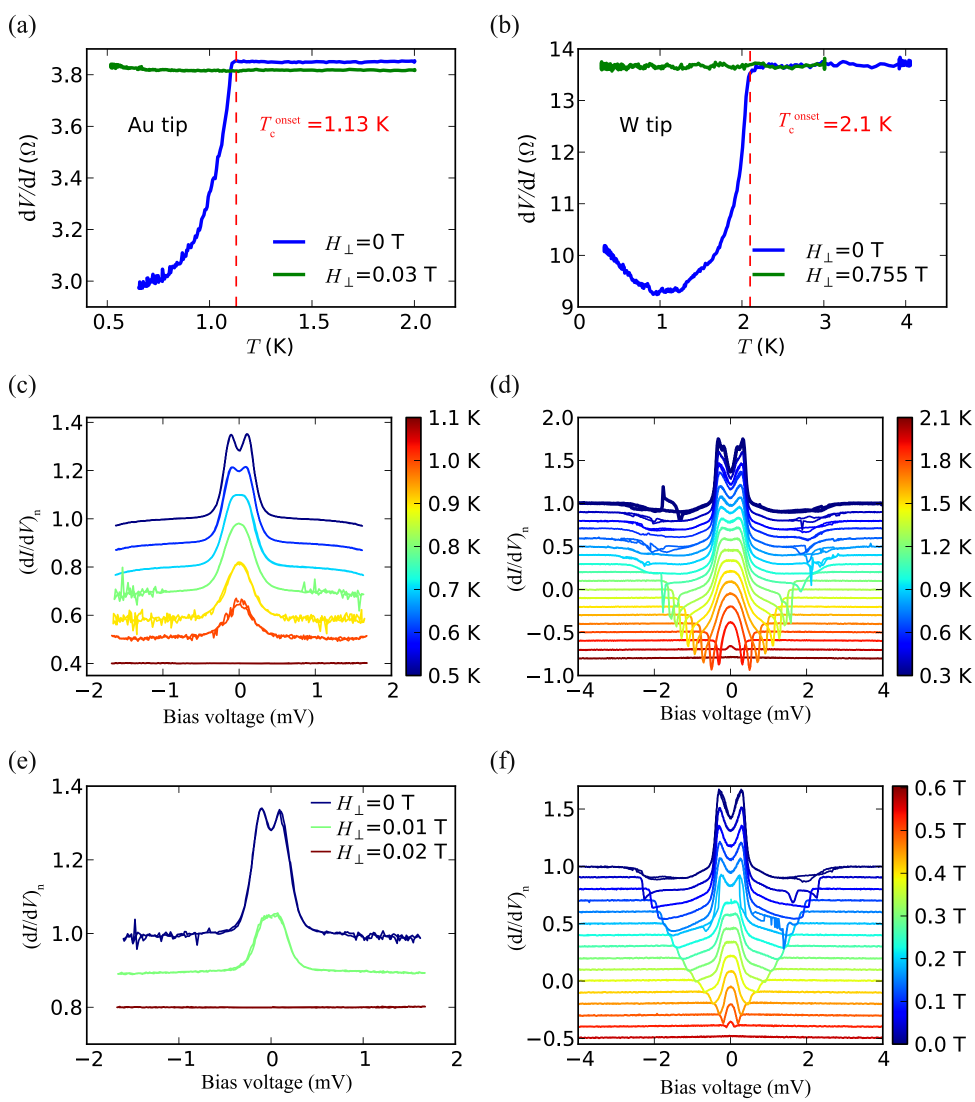

Fig. 16. Point contact results with the gold tip and the W tip. (a, b) The zero-bias point contact resistance as a function of temperature for the gold tip and the W tip, respectively; (c, d) the PCS at different T; (e and f) the PCS under different $H_\perp$ at 0.5 K; curves shifted in (c–f) for clarity. This figure is adapted from Ref. [23], Copyright @ 2017 Nature publishing group.

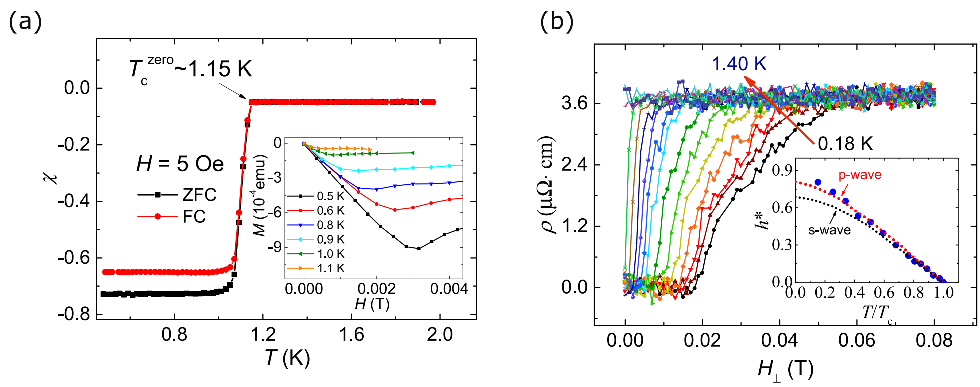

Fig. 17. Transport measurements of Au_2Pb. (a) Temperature dependence of χ, shows the Meissner effect: sharp diamagnetic drops at 1.15 K. The inset presents low-field M (H) curves at various temperatures from 0.5 to 1.1 K. (b) Magnetoresistance of Au_2Pb crystal at various temperatures under $H_\perp$. Inset: normalized upper critical field $h^* = H_{c2}/T_c(dH_{c2}/dT|_{T=Tc})$ as a function of normalized temperature $t = T/T_c$, with the red dashed line indicating the expectation for a polar p-wave state. This figure is adapted from Ref. [23], Copyright @ 2017 Nature publishing group.

shows double conductance peaks in the PCS at low temperature, which is absent in PCS under gold tip, implying the emergence of the new superconducting gap in Au_2Pb under the tungsten tip.

For exploring the origin of the TESC, the hardness of the tip material should be taken into consideration in particular. Compared to the gold tip, the tungsten tip can apply larger local pressure to the sample in the contact region with smaller deformation. Hence, it is natural to expect that the local pressure applied by hard tungsten tip seems to contribute to the TESC dominantly. This speculation is further confirmed by the first-principles calculations: comparing with the computed Fermi surfaces of Au_2Pb of relaxed lattice structure, the Fermi surfaces under 1% external uniaxial compression are found to be enlarged and the related density of states near the Fermi energy increases, which is consistent with the observed increase of T_c in the W/Au_2Pb point contact measurements. Besides the enhanced superconductivity by local pressure under the hard tip, the extremely enhanced H_{c2} in point contact may also be induced by structural defects and/or impurities at interface [39], resulting in the reduction of the mean free path l in the superconductor, which further leads to a decrease of the coherence length. Although the local pressure under the hard tip should contribute to the enhanced superconductivity in Au_2Pb, other effects arising from the hard point contact cannot be fully excluded, such as interface effect.

4.3. TESC in candidate of the chiral topological superconductor Sr_2RuO_4 single crystal

Since the discovery of the layered perovskite ruthenate Sr_2RuO_4 (SRO) by Maeno et al. at 1994 [114], many experimental measurements [115,116] have been performed on this material to investigate the possible chiral p-wave superconductivity predicted by Rice and Sigrist [117]. Until now, the expected local net magnetic field generated by the edge currents, as one smoking gun of chiral p-wave superconductivity, has not been directly observed with local field imaging [118]. However, the indirect evidence has already been revealed by point contact experiments [36,119], in which the magnetoresistance shows significant hysteresis which is often observed in ferromagnetic samples. This ferromagnetism-like behavior can be attributed to the time-reversal symmetry breaking field contributed by the edge current of the chiral domain. In addition, the in-plane tunneling junction of SRO also provides the evidence of surface Andreev bound state [120,121]. With this, the SRO is also proposed to host topological nature as a chiral quasi-2D superconductor by Sato and Ando [24].

Another promising result from the point contact experiment of SRO is the obvious T_c enhancement [36], namely TESC. The point contact is established on the a-b plain of SRO with a tungsten tip, and three point contact states are obtained by pressing the tip to the sample surface gradually, and show same energy scale of the zero bias conductance peaks with the value of 0.2 mV, a superconducting gap value as expected from the BCS weak-coupling theory. The most important thing to note is that superconducting features in the PCS can sustain even at the temperature higher than T_c of bulk SRO (1.5 K). In particular, the highest T_c of 6.5 K is observed in the point contact of 3.2 Ω (Fig. 18). Pressure experiments of SRO supply a wealth of information to investigate the origin of the TESC in SRO. The SRO is pressure sensitive materials: the T_c of SRO decreases in the hydrostatic pressure circumstance [122], while it is enhanced by applying an in-plane tensile along the ⟨1 0 0⟩ direction or a uniaxial pressure along the c axis [123–125]. The latter case proves that the pressure under the contact has contributions to the TESC in SRO. However, the T_c of TESC (~6.5 K) in SRO is almost twice of that obtained in uniaxial pressure experiment (~3.2 K), which indicates that some other effects may also play a role on the enhanced superconductivity for hard point contact measurement on SRO, like interface effect, etc.

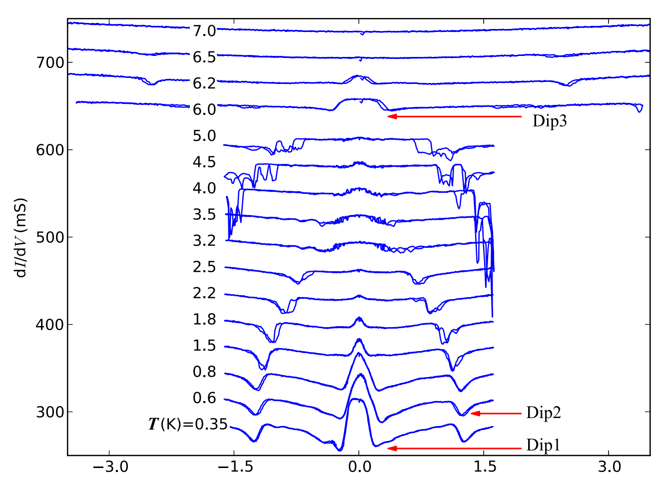

Fig. 18. The normalized PCS at different T for the point contact of $R_0 = 3.2\ \Omega$, the superconducting features totally vanish at 6.5 K. This figure is adapted from Ref. [36], Copyright @ 2015 American Physical Society.

5. Outlook and conclusions

5.1. The route to the development of TISC

Since the discovery of TISC in topological materials, the TISC is rapidly evolving from an experimental phenomenon to a new method to modulate physical properties. A typical application for this method is the search for topological superconductivity. As a powerful way to change a non-superconductor to superconductor, the TISC is just in its initial stage. In fact, a general theoretical model is still highly desired to describe the TISC although some theories on superconducting point contact can be referred, such as BTK model. Today, TISC faces challenges. How to improve its success rate? What is the definite origin of TISC in specific materials, such as TaAs? How to determine the pairing symmetry? What is the interface superconductivity in a mesoscopic contact region? etc. These challenges also offer the opportunities to further develop and expand the related experimental techniques: (i) Integrating with the tip enhanced Raman spectroscopy (TERS) in two-probe system. TERS is the combination of surface-enhanced Raman spectroscopy and scanning probe microscopy, which is carried out by a metal tip [126]. In this proposed system, one metal tip is used to induce the superconductivity in samples and the other tip for TERS is used to detect the variations of phonon modes near the contact. This can help analyze the distortion of the lattice structure of sample under the tip. (ii) Combining with STM in a two-probe system. The STM can map the spatial variation of superconducting order parameter, which would be helpful to determine the pairing symmetry and to confine the range of TISC in the sample. The STM tip itself can also carry out atomic point contact measurements [127–129]. (iii) Employing the ferromagnetic tips. It is well known that the ferromagnetism is always competitive with spin-singlet superconductivity, but compatible with the spin-triplet superconductivity, such as p-wave superconductivity [12,130]. Therefore, if superconductivity can be induced by a ferromagnetic tip, it prefers the p-wave pairing symmetry. (iv) Multi-probes for hard point contact measurements. The multiple TISC states can be induced simultaneously and mesoscopic superconductor-normal metal-superconductor junctions can be formed and measured. (v) Combining with pressure experiment. Uniaxial pressure experiment can be taken as a comparing experiment for TISC. It is helpful to determine and even quantize the contribution from the pressure. (vi) Combining with AFM mapping for modulating mesoscopic devices. By using AFM function, the target device can be located and then the AFM tip can be used as a hard point contact to modulate the physical properties of the device. Comparing to popular used gating method, the hard point contact offers another modulation way for microscale or nanoscale electronic devices.

5.2. Conclusions

In this review, we briefly introduce the background, history and present situations of TISC and TESC in topological materials. The former one is mainly realized in topological semimetals, such as Dirac semimetal Cd_3As_2 single crystal and Weyl semimetal TaAs single crystal. Both of them show double conductance peaks with double conductance dips and ZBCP, which is regarded as the typical feature of p-wave superconductivity and the Majorana zero mode. These spectroscopic evidences of topological superconductivity not only live up to the expectations of potential application in fault-tolerated topological computations but also provide a deeper insight into the understanding of superconductivity. The TESC opens a new route to locally modulate superconducting properties. The enhanced superconducting state under the tip can be investigated by detecting the superconducting parameters, such as the magnitude of the superconducting gap, the T_c value, the H_{c2} value, the cooper pairing symmetry, and the energy of electron-quasiparticle couplings. It has been proved that hard point contact can be taken as a complementary experimental method to explore unconventional superconductivity especially for topological superconductivity with STM, pressure and gating techniques. Please notice that the hard point contact modulation is not only applicable for the research on superconductivity but also expected to tune other physical phases or phase transitions in both bulk and nano systems, like ferromagnetic or anti-ferromagnetic properties.

Conflict of interest

The authors declare that they have no conflict of interest.

Acknowledgments

We acknowledge Jian Wei for the contribution to the hard point contact measurements and Yu. G. Naidyuk for some corrections on the manuscript. This work was financially supported by the National Program on Key Basic Research Project (2018YFA0305604 and 2017YFA0303302), National Natural Science Foundation of China (11774008, 381/0401210001), the Key Research Program of the Chinese Academy of Sciences (XDPB08-2), the Open Research Fund Program of the State Key Laboratory of Low-Dimensional Quantum Physics, Tsinghua University (KF201703), and China Postdoctoral Science Foundation (130/0401130005).

References

[1] Read N, Green D. Paired states of fermions in two dimensions with breaking of parity and time-reversal symmetries and the fractional quantum Hall effect. Phys Rev B 2000;61:10267.
[2] Kitaev AY. Unpaired Majorana fermions in quantum wires. Phys Usp 2001;44:131–6.
[3] Ivanov DA. Non-Abelian statistics of half-quantum vortices in p-wave superconductors. Phys Rev Lett 2001;86:268–71.
[4] Hasan MZ, Kane CL. Colloquium: topological insulators. Rev Mod Phys 2010;82:3045–67.
[5] Qi XL, Zhang SC. Topological insulators and superconductors. Rev Mod Phys 2011;83:1057–110.
[6] Fu L, Kane CL. Superconducting proximity effect and Majorana fermions at the surface of a topological insulator. Phys Rev Lett 2008;100:096407.
[7] Alicea J. New directions in the pursuit of Majorana fermions in solid state systems. Rep Prog Phys 2012;75:076501.
[8] Nayak C, Simon SH, Stern A, et al. Non-Abelian anyons and topological quantum computation. Rev Mod Phys 2008;80:1083–159.
[9] Alicea J, Oreg Y, Refael G, et al. Non-Abelian statistics and topological quantum information processing in 1D wire networks. Nat Phys 2011;7:412–7.
[10] Liu XJ, Wong CLM, Law KT. Non-Abelian Majorana doublets in time-reversal-invariant topological superconductors. Phys Rev X 2014;4:021018.
[11] Wang J, Shi CT, Tian ML, et al. Proximity-induced superconductivity in nanowires: minigap state and differential magnetoresistance oscillations. Phys Rev Lett 2009;102:247003.
[12] Wang J, Singh M, Tian ML, et al. Interplay between superconductivity and ferromagnetism in crystalline nanowires. Nat Phys 2010;6:389–94.
[13] Wang J, Chang CZ, Li HD, et al. Interplay between topological insulators and superconductors. Phys Rev B 2012;85:045415.
[14] Mourik V, Zuo K, Frrolov SM, et al. Signatures of Majorana fermions in hybrid superconductor- semiconductor nanowire devices. Science 2012;336:1003–7.
[15] Deng MT, Yu CL, Huang GY, et al. Observation of Majorana fermions in a Nb-InSb nanowire-Nb hybrid quantum device. Nano Lett 2012;12:6414–9.
[16] Das A, Ronen Y, Most Y, et al. Zero-bias peaks and splitting in an Al-InAs nanowire topological superconductor as a signature of Majorana fermions. Nat Phys 2012;8:887–95.
[17] Sun HH, Zhang KW, Hu LH, et al. Majorana zero mode detected with spin selective Andreev reflection in the vortex of a topological superconductor. Phys Rev Lett 2016;116:257003.
[18] Nadj-Perge S, Drozdov IK, Li J, et al. Observation of Majorana fermions in ferromagnetic atomic chains on a superconductor. Science 2014;346:602–7.

[19] Zhang DM, Wang J, DaSilva AM, et al. Superconducting proximity effect and possible evidence for pearl vortices in a candidate topological insulator. Phys Rev B 2011;84:165120.
[20] Yang F, Ding Y, Qu FM, et al. Proximity effect at superconducting Sn-Bi_2Se_3 interface. Phys Rev B 2012;85:104508.
[21] Sasaki S, Kriener M, Segawa K, et al. Topological superconductivity in $Cu_xBi_2Se_3$. Phys Rev Lett 2011;107:217001.
[22] Wray LA, Xu SY, Xia YQ, et al. Observation of topological order in a superconducting doped topological insulator. Nat Phys 2010;6:855.
[23] Xing Y, Wang H, Li CK, et al. Superconductivity in topologically nontrivial material Au_2Pb. npj. Quant Mater 2016;1:16005.
[24] Sato M, Ando Y. Topological superconductors: a review. Rep Prog Phys 2017;80:076501.
[25] Qi YP, Naumov PG, Ali MN, et al. Superconductivity in Weyl semimetal candidate $MoTe_2$. Nat Commun 2016;7:11038.
[26] Guguchia Z, Rohr VF, Shermadini Z, et al. Signatures of the topological s^{+-} superconducting order parameter in the type-II Weyl semimetal T_d-$MoTe_2$. Nat Commun 2017;8:1082.
[27] Lv YF, Wang WL, Zhang YM, et al. Experimental signature of topological superconductivity and Majorana zero modes on β-Bi_2Pd thin films. Sci Bull 2017;62:852–6.
[28] Wang H, Wang HC, Liu HW, et al. Observation of superconductivity induced by a point contact on 3D Dirac semimetal Cd_3As_2 crystals. Nat Mater 2016;15:38–42.
[29] Aggarwal L, Gaurav A, Thakur GS, et al. Unconventional superconductivity at mesoscopic point contacts on the 3D Dirac semimetal Cd_3As_2. Nat Mater 2016;15:32–7.
[30] Wang H, Wang HC, Chen YQ, et al. Discovery of tip induced unconventional superconductivity on Weyl semimetal. Sci Bull 2017;62:425–30.
[31] Aggarwal L, Gayen S, Das S, et al. Mesoscopic superconductivity and high spin polarization coexisting at metallic point contacts on Weyl semimetal TaAs. Nat Commun 2017;8:13974.
[32] Das S, Aggarwal L, Roychowdhury S, et al. Unexpected superconductivity at nanoscale junctions made on the topological crystalline insulator $Pb_{0.6}Sn_{0.4}Te$. Appl Phys Lett 2016;109:132601.
[33] Naidyuk YG, Yanson IK. Point-contact spectroscopy. Monograph: Springer; 2005.
[34] Gloos K, Martin F, Schank C, et al. Pressure effects in point contacts with heavy-fermion $CeCu_2Ge_2$. Phys B 1995;206&207:279–81.
[35] Yin JX, Wang JH, Wu Z, et al. Tip-pressure-induced incoherent energy gap in $CaFe_2As_2$. Chin Phys Lett 2016;33:067401.
[36] Wang H, Lou WJ, Luo JW, et al. Enhanced superconductivity at the interface of W/Sr_2RuO_4 point contacts. Phys Rev B 2015;91:184514.
[37] Shklyarevskii OI, Duif AM, Jansen AGM, et al. Superconductivity in Bi observed with point contacts. Phys Rev B 1986;34:1956.
[38] Shklyarevskii OI, Gribov NN, Naidyuk YG. Electron-phonon interaction in gallium point contacts. Fiz Nizk Temp 1983;9:1068–77.
[39] Naidyuk YG, Lohneysen HV, Yanson IK. Temperature and magnetic-field dependence of the superconducting order parameter in Zn studied by point-contact spectroscopy. Phys Rev B 1996;54:16077.
[40] Ji Y, Chien CL, Stiles MD. Current-induced spin-wave excitations in a single ferromagnetic layer. Phys Rev Lett 2003;90:106601.
[41] Duif AM, Jansen AGM, Wyder P. Point-contact spectroscopy. J Phys Condens Matter 1989;l:3157–89.
[42] Naidyuky YG, Yanson IK. Point-contact spectroscopy of heavy-fermion systems. J Phys Condens Matter 1998;10:8905–38.
[43] Deutsche G. Andreev–Saint-James reflections: a probe of cuprate superconductors. Rev Mod Phys 2005;77:109.
[44] Daghero D, Gonnelli RS. Probing multiband superconductivity by point-contact spectroscopy. Supercond Sci Technol 2010;23:043001.
[45] Park WK, Greene LH. Andreev reflection and order parameter symmetry in heavy-fermion superconductors: the case of $CeCoIn_5$. J Phys Condens Matter 2009;21:103203.
[46] Yanson IK. Nonlinear effect in electric conductivity of point junctions and electron-phonon interaction in normal metals. Sov Phys JETP 1974;39:506–13.
[47] Moreland J, Ekin JW. Electron tunneling experiments using Nb-Sn 'break' junctions. J Appl Phys 1985;58:3888.
[48] Ralls KS, Buhrman RA, Tiberio RC. Fabrication of thin-film metal nanobridges. Appl Phys Lett 1989;55:2459.
[49] Myers EB, Ralph DC, Katine JA, et al. Current-induced switching of domains in magnetic multilayer devices. Science 1999;285:867–70.
[50] Jansen AG, Mueller FM, Wyder P. Normal metallic point contacts. Science 1978;199:1037–40.
[51] Sharvin YV. A possible method for studying Fermi surfaces. J Exptl Theoret Phys (USSR) 1965;48:984–5.
[52] Andreev AF. Thermal conductivity of the intermediate state of superconductors. Sov Phys JETP 1964;19:1228.
[53] Wexler G. The size effect and the non-local Boltzmann transport equation in orifice and disk geometry. Proc Phys Soc 1966;89:927.
[54] Wang CM, Lu HZ, Shen SQ. Anomalous phase shift of quantum oscillations in 3D topological semimetals. Phys Rev Lett 2016;117:077201.
[55] Murakawa H, Bahramy MS, Tokunaga M, et al. Detection of Berry's phase in a bulk Rashba semiconductor. Science 2013;342:1490–3.
[56] Akimenko AI, Verkin AB, Ponomarenko NM, et al. Point contact spectroscopy of copper-temperature-measurements, dependence of the point contact spectra on the contact parameters. Sov J Low Temp Phys 1982;8:130.
[57] Blonder GE, Tinkham M, Klapwijk TM. Transition from metallic to tunneling regimes in superconducting microconstructions: excess current, charge imbalance, and supercurrent conversion. Phys Rev B 1982;25:4515.
[58] Srikanth H, Raychaudhuri AK. Modeling tunneling data of normal metal-oxide superconductor point contact junctions. Physica C 1992;190: 229–33.
[59] Pleceník A, Grajcar M, Beňačka Š, et al. Finite-quasiparticle-lifetime effects in the differential conductance of $Bi_2Sr_2CaCu_2O_y$/Au junctions. Phys Rev B 1994;49:10016.
[60] Tanaka Y, Kashiwaya S. Theory of tunneling spectroscopy of d-wave superconductors. Phys Rev Lett 1995;74:3451.
[61] Yamashiro M, Tanaka Y, Kashiwaya S. Theory of tunneling spectroscopy in superconducting Sr_2RuO_4. Phys Rev B 1997;56:7847.
[62] Tinkham M. Introduction to superconductivity. 2nd ed. McGraw-Hill, Inc; 1996.
[63] Morenzoni E, Saadaoui H, Amato A, et al. Field dependence of the superconducting gap inYPd_2Sn: a μSR and NMR study. J Phys Conf Ser 2014;551:012027.
[64] Soulen RJ, Byers JM, Osofsky MS, et al. Measuring the spin polarization of a metal with a superconducting point contact. Science 1998;282:85.
[65] Guan T, Lin CJ, Yang CL, et al. Evidence for half-metallicity in n-type $HgCr_2Se_4$. Phys Rev Lett 2015;115:087002.
[66] Buzea C, Robbie K. Assembling the puzzle of superconducting elements: a review. Supercond Sci Technol 2005;18:R1.
[67] Shimizu K, Amaya K, Suzuki N. Pressure-induced Superconductivity in elemental materials. J Phys Soc Jpn 2005;74:1345–57.
[68] Li YF, Zhou YH, Guo ZP, et al. Concurrence of superconductivity and structure transition in Weyl semimetal TaP under pressure. npj Quant Mater 2017;2:66.
[69] Bednorz JG, Muller KA. Possible high T_c superconductivity in the Ba-La-Cu-O system. Z Phys B 1986;64:189.
[70] Schrieffer JR, Brooks JS. Handbook of high-temperature superconductivity. New York: Springer Science+Business Media; 2007.
[71] He LP, Jia YT, Zhang SJ, et al. Pressure-induced superconductivity in the three-dimensional topological Dirac semimetal Cd_3As_2. npj Quant Mater 2016;1:16014.
[72] Wang QY, Li Z, Zhang WH, et al. Interface-induced high-temperature superconductivity in single unit-cell FeSe films on $SrTiO_3$. Chin Phys Lett 2012;29:037402.
[73] Zhang WH, Sun Y, Zhang JS, et al. Direct observation of high-temperature superconductivity in one-unit-cell FeSe films. Chin Phys Lett 2014;31:017401.
[74] Wang ZQ, Liu CF, Liu Y, et al. High-temperature superconductivity in one-unit-cell FeSe film. J Phys Condens Matter 2017;29:153001.
[75] Ying X, Wang J. Direct evidence of high temperature superconductivity in one-unit-cell FeSe films on $SrTiO_3$ substrate by transport and magnetization measurements. Chin Phys B 2015;24:117404.
[76] Huang D, Hoffman JE. Monolayer FeSe on $SrTiO_3$. Annu Rev Condens Matter Phys 2017;8:311–36.
[77] Pereiro J, Petrovic A, Panagopoulos C, et al. Interface superconductivity: history, development and prospects. Phys Express 2011;1:208.
[78] Gariglio S, Gabay M, Mannhart J, et al. Interface superconductivity. Physica C 2015;514:189–98.
[79] Reyren N, Thiel S, Cavigli AD, et al. Superconducting interfaces between insulating oxides. Science 2007;317:1196–9.
[80] Shen SC, Xing Y, Wang PJ, et al. Observation of quantum Griffiths singularity and ferromagnetism at the superconducting $LaAlO_3/SrTiO_3$ (110) interface. Phys Rev B 2016;94:144517.
[81] Ohtomo A, Muller DA, Grazul JL, et al. Artificial charge-modulation in atomic-scale perovskite titanate superlattices. Nature 2002;419:378–80.
[82] Gozar A, Logvenov G, Kourkoutis FL, et al. High-temperature interface superconductivity between metallic and insulating copper oxides. Nature 2008;455:782–5.
[83] Zhou YH, Lu PC, Du YP, et al. Pressure-induced new topological Weyl semimetal phase in TaAs. Phys Rev Lett 2016;117:146402.
[84] Young SM, Zaheer S, Teo JCY, et al. Dirac semimetal in three dimensions. Phys Rev Lett 2012;108:140405.
[85] Wang ZJ, Weng HM, Wu QS, et al. Three-dimensional Dirac semimetal and quantum transport in Cd_3As_2. Phys Rev B 2013;88:125427.
[86] Wan XG, Turner AM, Vishwanath A, et al. Topological semimetal and Fermi-arc surface states in the electronic structure of pyrochlore iridates. Phys Rev B 2011;83:205101.
[87] Liu ZK, Zhou B, Zhang Y, et al. Discovery of a three-dimensional topological Dirac semimetal Na_3Bi. Science 2014;343:864–7.
[88] Ali MN, Gibson Q, Jeon S, et al. The crystal and electronic structures of Cd_3As_2, the three-dimensional electronic analogue of graphene. Inorg Chem 2014;53:4062.
[89] Liu ZK, Jiang J, Zhou B, et al. A stable three-dimensional topological Dirac semimetal Cd_3As_2. Nat Mater 2014;13:677–81.
[90] Jeon S, Zhou BB, Gyenis A, et al. Landau quantization and quasiparticle interference in the three-dimensional Dirac semimetal Cd_3As_2. Nat Mater 2014;13:851.

[91] Zhao YF, Liu HW, Zhang CL, et al. Anisotropic Fermi surface and quantum limit transport in high mobility three-dimensional Dirac semimetal Cd_3As_2. Phys Rev X 2015;5:031037.
[92] Tian L, Quinn G, Mazhar NA, et al. Ultrahigh mobility and giant magnetoresistance in the Dirac semimetal Cd_3As_2. Nat Mater 2015;14:280–4.
[93] Kobayashi S, Sato M. Topological superconductivity in Dirac semimetals. Phys Rev Lett 2015;115:187001.
[94] Burkov AA, Balents L. Weyl semimetal in a topological insulator multilayer. Phys Rev Lett 2011;107:127205.
[95] Xu G, Weng HM, Wang Z, et al. Chern semimetal and the quantized anomalous Hall effect in $HgCr_2Se_4$. Phys Rev Lett 2011;107:186806.
[96] Weng H, Fang C, Fang Z, et al. Weyl semimetal phase in noncentrosymmetric transition-metal monophosphides. Phys Rev X 2015;5:011029.
[97] Huang SM, Xu SY, Belopolski I, et al. A Weyl fermion semimetal with surface Fermi arcs in the transition metal monopnictide TaAs class. Nat Commun 2015;6:7373.
[98] Xu SY, Beloposki I, Alidoust N, et al. Discovery of a Weyl fermion semimetal and topological Fermi arcs. Science 2015;349:613–7.
[99] Lv BQ, Weng HM, Fu BB, et al. Experimental discovery of Weyl semimetal TaAs. Phys Rev X 2015;5:031013.
[100] Lv BQ, Xu N, Weng HM, et al. Observation of Weyl nodes in TaAs. Nat Phys 2015;11:724–7.
[101] Huang XC, Zhao LX, Long YJ, et al. Observation of the chiral-anomaly-induced negative magnetoresistance in 3D Weyl semimetal TaAs. Phys Rev X 2015;5:031023.
[102] Zhang CL, Xu SY, Belopolski I, et al. Signatures of the Adler–Bell–Jackiw chiral anomaly in a Weyl fermion semimetal. Nat Commun 2016;7:10735.
[103] Wang HC, Li CK, Liu HW, et al. Chiral anomaly and ultrahigh mobility in crystalline $HfTe_5$. Phys Rev B 2016;93:165127.
[104] Jia S, Xu SY, Hasan MZ. Weyl semimetals, Fermi arcs and chiral anomalies. Nat Mater 2016;15:1140–4.
[105] Aoki D, Huxley A, Ressouche E, et al. Coexistence of superconductivity and ferromagnetism in URhGe. Nature 2001;413:613.
[106] Liu Y, Wang ZQ, Zhang XF, et al. Interface-induced Zeeman-protected superconductivity in ultrathin crystalline Lead films. Phys Rev X 2018;8:021002.
[107] Sheet G, Mukhopadhyay S, Raychaudhuri P. Role of critical current on the point-contact Andreev reflection spectra between a normal metal and a superconductor. Phys Rev B 2004;69:134507.
[108] Reyren N, Gariglio S, Caviglia AD, et al. Anisotropy of the superconducting transport properties of the $LaAlO_3/SrTiO_3$ interface. Appl Phys Lett 2009;94:112506.
[109] Levy M, Olsen JL. Can pressure destroy superconductivity in aluminum? Solid State Commun 1964;2:137–9.
[110] Hamilton DC, Raub CH, Matthias BT. Some new superconducting compounds. J Phys Chem Solids 1965;26:665–7.
[111] Schoop LM, Xie LS, Chen R, et al. Dirac metal to topological metal transition at a structural phase change in Au_2Pb and prediction of Z_2 topology for the superconductor. Phys Rev B 2015;91:214517.
[112] Yu YJ, Xu Y, Xing Y, et al. Fully gapped superconducting state in Au_2Pb: a natural candidate for topological superconductor. Europhys Lett 2016;116:67002.
[113] Chen KW, Graf D, Besara T, et al. Temperature-pressure phase diagram of cubic Laves phase Au_2Pb. Phys Rev B 2016;93:045118.
[114] Maeno Y, Hashimoto H, Yoshida K, et al. Superconductivity in a layered perovskite without copper. Nature 1994;372:532–4.
[115] Mackenzie AP, Maeno Y. The superconductivity of Sr_2RuO_4 and the physics of spin-triplet pairing. Rev Mod Phys 2003;75:657.
[116] Maeno Y, Kittaka S, Nomura T, et al. Evaluation of spin-triplet superconductivity in Sr_2RuO_4. J Phys Soc Jpn 2012;81:011009.
[117] Rice TM, Sigrist M. Sr_2RuO_4: an electronic analogue of ^3He? J Phys Condens Matter 1995;7:L643–8.
[118] Curran PJ, Bending SJ, Desoky WM, et al. Search for spontaneous edge currents and vortex imaging in Sr_2RuO_4 mesostructures. Phys Rev B 2014;89:144504.
[119] Wang H, Luo JW, Lou WJ, et al. Probing chiral superconductivity in Sr_2RuO_4 underneath the surface by point contact measurements. New J Phys 2017;19:053001.
[120] Kashiwaya S, Kashiwaya H, Kambara H, et al. Edge states of Sr_2RuO_4 detected by in-plane tunneling spectroscopy. Phys Rev Lett 2011;107:077003.
[121] Kashiwaya S, Kashiwaya H. Saitoh K et al Tunneling spectroscopy of topological superconductors. Physica E 2014;55:25–9.
[122] Shirakawa N, Murataγ K, Nishizaki S, et al. Pressure dependence of superconducting critical temperature of Sr_2RuO_4. Phys Rev B 1997;56:7890.
[123] Kittaka S, Taniguchi H, Yonezawa S, et al. Higher-T_c superconducting phase in Sr_2RuO_4 induced by uniaxial pressure. Phys Rev B 2010;81:180510.
[124] Kittaka S, Yaguchi H, Maeno Y. Large enhancement of 3-K phase superconductivity in the Sr_2RuO_4-Ru eutectic system by uniaxial pressure. J Phys Soc Jpn 2009;78:103705.
[125] Hicks CW, Brodsky DO, Yelland EA, et al. Strong increase of T_c of Sr_2RuO_4 under both tensile and compressive strain. Science 2014;344:283.
[126] Kumar N, Mignuzzi S, Su WT, et al. Tip-enhanced Raman spectroscopy: principles and applications. EPJ Techniq Instrum 2015;2:9.
[127] Smith DPE. Quantum point contact switches. Science 1995;269:371.
[128] Kim H, Hasegawa Y. Site-dependent evolution of electrical conductance from tunneling to atomic point contact. Phys Rev Lett 2015;114:206801.
[129] Hou XY, Jie YY, Gong J, et al. Transition from tunneling regime to local point contact realized on $Ba_{0.6}K_{0.4}Fe_2A_{s2}$ surface. Chin Phys B 2017;26:6.
[130] Fay D, Appel J. Coexistence of p-state superconductivity and itinerant ferromagnetism. Phys Rev B 1980;22:7.

He Wang received his B.S. degree from Tianjin University in 2007 and Ph.D. degree in physics in 2016 from Peking University. He was a postdoc at Tianjin international center of nano-particle and nano-system in Tianjin University from 2016 to 2018. Dr. Wang joined Department of Physics in Capital Normal University as a faculty member in July, 2018.

Lei Ma earned his Ph.D. degree in 2010. Then he had his Postdoc training in Brown University and Georgia tech. From 2016, he took a full professor position in Tianjin University as a Beiyang outstanding oversea scholar and Tianjin 1000 Talent youth scholar. His research mainly focuses on graphene electronics related physics and cluster physics as well as the instrumentation of mass spectrometer and high resolution photo-electrometer.

Jian Wang received his B.S. degree from Shandong University in 2001 and Ph.D. degree from Institute of Physics, Chinese Academy of Sciences in 2007. He is now a Changjiang Distinguished Professor at International Center for Quantum Materials, School of Physics, Peking University. His current research interest is mainly focused on the physical properties of low dimensional superconductors and topological materials.